JOURNAL OF GEOPHYSICAL RESEARCH: OCEANS, VOL. 118, 2774–2792, doi:10.1002/jgrc.20217, 2013

Rates and mechanisms of turbulent dissipation and mixing in the Southern Ocean: Results from the Diapycnal and Isopycnal Mixing Experiment in the Southern Ocean (DIMES)

K. L. Sheen,[1] J. A. Brearley,[1] A. C. Naveira Garabato,[1] D. A. Smeed,[2] S. Waterman,[3] J. R. Ledwell,[4] M. P. Meredith,[5] L. St. Laurent,[4] A. M. Thurnherr,[6] J. M. Toole,[4] and A. J. Watson[7]

Received 27 November 2012; revised 19 April 2013; accepted 19 April 2013; published 4 June 2013.

[1] The spatial distribution of turbulent dissipation rates and internal wavefield characteristics is analyzed across two contrasting regimes of the Antarctic Circumpolar Current (ACC), using microstructure and finestructure data collected as part of the Diapycnal and Isopycnal Mixing Experiment in the Southern Ocean (DIMES). Mid-depth turbulent dissipation rates are found to increase from $O\left(1 \times 10^{-10}\ \mathrm{W\ kg^{-1}}\right)$ in the Southeast Pacific to $O\left(1 \times 10^{-9}\ \mathrm{W\ kg^{-1}}\right)$ in the Scotia Sea, typically reaching $3 \times 10^{-9}\ \mathrm{W\ kg^{-1}}$ within a kilometer of the seabed. Enhanced levels of turbulent mixing are associated with strong near-bottom flows, rough topography, and regions where the internal wavefield is found to have enhanced energy, a less-inertial frequency content and a dominance of upward propagating energy. These results strongly suggest that bottom-generated internal waves play a major role in determining the spatial distribution of turbulent dissipation in the ACC. The energy flux associated with the bottom internal wave generation process is calculated using wave radiation theory, and found to vary between 0.8 mW $\mathrm{m^{-2}}$ in the Southeast Pacific and 14 mW $\mathrm{m^{-2}}$ in the Scotia Sea. Typically, 10%–30% of this energy is found to dissipate within 1 km of the seabed. Comparison between turbulent dissipation rates inferred from finestructure parameterizations and microstructure-derived estimates suggests a significant departure from wave-wave interaction physics in the near-field of wave generation sites.

Citation: Sheen, K. L., et al. (2013) Rates and mechanisms of turbulent dissipation and mixing in the Southern Ocean: Results from the Diapycnal and Isopycnal Mixing Experiment in the Southern Ocean (DIMES), *J. Geophys. Res. Oceans*, *118*, 2774–2792, doi:10.1002/jgrc.20217.

1. Introduction

[2] Turbulent mixing processes in the Southern Ocean are believed to play an important role in determining the oceanic overturning circulation and influencing the Earth's climate system. Several reasons underpin this belief. Small-scale turbulent motions, which diffusively mix water properties across density surfaces, are centrally implicated in balancing the diapycnal upwelling of deep waters that flow in the overturning circulation [e.g., *Munk and Wunsch*, 1998; *Lumpkin and Speer*, 2007; *Naveira Garabato et al.*, 2007; *Zika et al.*, 2009]. Furthermore, small-scale turbulence provides the route through which energy input to the global ocean circulation by wind, tides, and surface buoyancy forcing is dissipated. The importance of Southern Ocean mixing reflects the large rate at which energy is locally imparted to the ocean by the strong westerly winds that circulate around Antarctica; these force the Antarctic Circumpolar Current (ACC) on both subinertial and near-inertial timescales [*Wunsch*, 1998; *Alford*, 2003; *Scott and Xu*, 2009].

[3] In the last decade, several studies have highlighted the significance of turbulent mixing processes in the Southern Ocean. These studies include (i) indirect estimates of the rates of turbulent kinetic energy dissipation, ϵ, and diapycnal diffusivity, K_ρ, by the application of finescale parameterizations to internal wave velocity and density finestructure measured on vertical scales of O(10–100 m) and (ii) the application of internal wave radiation theory to

[1]Ocean and Earth Science, University of Southampton, National Oceanography Centre Southampton, European Way, Southampton, UK.
[2]Marine Physics and Ocean Climate, National Oceanography Centre Southampton, European Way, Southampton, UK.
[3]Climate Change Research Centre and ARC Centre of Excellence for Climate System Science, University of New South Wales, Sydney, New South Wales, Australia.
[4]Applies Ocean Physics and Engineering, Woods Hole Oceanographic Institution, Woods Hole, Massachusetts, USA.
[5]Polar Oceans, British Antarctic Survey, Madingley Road High Cross Cambridge Cambridgeshire, UK.
[6]Ocean and Climate Physics, Lamont-Doherty Earth Observatory, Palisades, New York, USA.
[7]School of Environmental Sciences, University of East Anglia, Norwich, UK.

Corresponding author: K. L. Sheen, University of Southampton, National Oceanography Centre Southampton, European Way, Southampton, SO14 3ZH, UK. (k.sheen@soton.ac.uk)

2169-9275/13/10.1002/jgrc.20217

measurements of small-scale (O(1–10 km)) topographic roughness alongside near-bottom velocity and stratification data to estimate the rate of internal wave radiation. These calculations have yielded significant insights into the physical pathways between the large-scale energy input and the small-scale turbulent dissipation in the Southern Ocean, pointing to the potentially pivotal role of internal waves. On the basis of these indirect studies, it has been suggested that turbulent dissipation and mixing in the Southern Ocean are primarily underpinned by the breaking of internal lee waves generated as deep-reaching geostrophic flows impinge on rough sea-floor topography [*Naveira Garabato et al*., 2004; *Sloyan*, 2005; *Kunze et al*., 2006; *Nikurashin and Ferrari*, 2010a; *Wu et al*., 2011] and that this process contributes significantly to the energy budget and dynamical balance of the Southern Ocean [*Nikurashin and Ferrari*, 2010b, 2011; *Scott et al*., 2011; *Naveira Garabato et al*., 2013]. The key message of those studies is that topographically rough sectors of the Southern Ocean likely host the generation and breaking of internal waves at rates that are comparable to the wind work over the ACC (typically $\sim$10 mW m^{-2}, *Wunsch* [1998]) with associated deep-ocean turbulent diapycnal diffusivities of $O(10^{-4}-10^{-3}$ m^2 s$^{-1})$, elevated over characteristic oceanic background levels by at least an order of magnitude.

[4] The Diapycnal and Isopycnal Experiment in the Southern Ocean (DIMES) was instigated to test these concepts as well as current ideas on the physical controls of isopycnal stirring across the ACC. DIMES revolves around a large program of fieldwork measurements spanning two contrasting sectors of the ACC (the southeast Pacific and southwest Atlantic). The fieldwork includes a tracer release experiment on an isopycnal embedded within the Circumpolar Deep Water that upwells across the Southern Ocean [*Ledwell et al*., 2011] (A. J. Watson et al., Direct measurement of rapid cross-density ocean mixing at mid depths in Drake Passage?, submitted to *Nature*, 2013)); the deployment of swarms of isopycnal floats, surface drifters, and profiling Electromagnetic Autonomous Profiling Explorer (EM-APEX) floats [*Sanford et al*., 2005], to investigate lateral stirring processes and the upper-ocean internal wavefield; the deployment of a six mooring cluster in Drake Passage for 2 years to study the interaction of the Southern Ocean eddy field with small-scale topography and the internal wavefield (J. A. Brearley et al., Subinertial modulation of turbulent mixing east of Drake Passage, submitted to *Journal of Physical Oceanography*, 2013, hereinafter referred to as Brearley et al., submitted manuscript, 2013); and the acquisition of fine- and microstructure profiles to assess the rates of turbulent dissipation and mixing, as well as their underpinning mechanisms [*St. Laurent et al*., 2012].

[5] Here, we use the fine- and microstructure measurements collected during the first 3 years of DIMES to assess our present view of the role of small-scale turbulence in the Southern Ocean circulation, outlined earlier. We do this by analyzing the spatial distribution of turbulent dissipation and mixing throughout the DIMES study region and quantitatively examining how it relates to the properties of the internal wavefield, background flow and stratification, and small-scale topography. Our analysis follows that of *St. Laurent et al*. [2012], who discuss a subset of the data set analyzed here, and of *Waterman et al*. [2012] and S. Waterman et al. (Suppression of internal wave breaking by lee wave-mean flow interactions in the Antarctic Circumpolar Current?, submitted to *Journal of Physical Oceanography*, 2012, hereinafter referred to as Waterman et al., submitted manuscript, 2012), who investigate similar issues using a more modest collection of fine- and microstructure observations across the ACC standing meander north of the Kerguelen Plateau. Section 2 provides an overview of data collection and processing methods. Section 3 presents microstructure-derived estimates of turbulent dissipation and mixing, alongside finestructure-derived metrics of key internal wave characteristics along four cross-ACC transects in the DIMES study region. The generation of internal waves as the ACC flow impinges on seafloor topography and their subsequent evolution are, respectively, discussed in sections 4 and 5, in light of wave-radiation theory and other theoretical considerations. Section 6 summarizes the main findings and outstanding questions arising from this work.

2. Methods

2.1. Data Acquisition

[6] This study analyzes microstructure and finestructure data from four meridional cross-ACC transects collected between March 2010 and April 2011 (Figure 1a). The westernmost transect (T1), at $\sim$78°W, is located in the southeast Pacific above a relatively smooth oceanic seafloor, with root-mean-square bathymetric height variations, H, of 10–100 m. ACC near-bottom current speeds here are typically 0.05 m s^{-1}. Transects T2–T4 are located further downstream, where the ACC is channeled through the 700 km wide Drake Passage and into the Scotia Sea. Here, bottom flows reach up to 0.5 m s^{-1} and encounter a series of topographic ridges and other complex bathymetry, remnants of a once extensive sea-floor spreading region ($H \sim$ 100–300m). Transect T2, which runs across western Drake Passage, is a repeat of the World Ocean Circulation Experiment (WOCE) section A21 [*Roether et al*., 1993]. Transect T3 is located along the underwater mountain chain of the Phoenix ridge at 66°W, while transect T4 is aligned with the WOCE SR1b repeat line [*Meredith et al*., 2011]. Together, the four transects span a region that exhibits significant variations in both topographic roughness and bottom current velocities (Figure 2). Data presented here were collected during three DIMES surveys. Transect T3 was obtained in March 2010 onboard *R/V Thomas G. Thompson* (US2 cruise); transects T1 and T2 were performed between December 2010 and January 2011 on the *RRS James Cook* (UK2 cruise); transect T4 was undertaken in April 2011 onboard the *RRS James Clark Ross* (UK2.5 cruise). Cruise reports can be found online at http://dimes.ucsd.edu/results. In total, 75 stations are analyzed, of which 37 contain both microstructure and finestructure data.

2.2. Microstructure

[7] The principal metric of diapycnal mixing that we investigate is the rate of turbulent energy dissipation, ϵ, measured in W kg^{-1}. Here, ϵ was determined directly using free-falling vertical microstructure profilers (VMPs). These instruments record velocity shear ($\partial u/\partial z$) and temperature variance on centimeter scales. Assuming isotropy, the dissipation rate of turbulent energy is given by

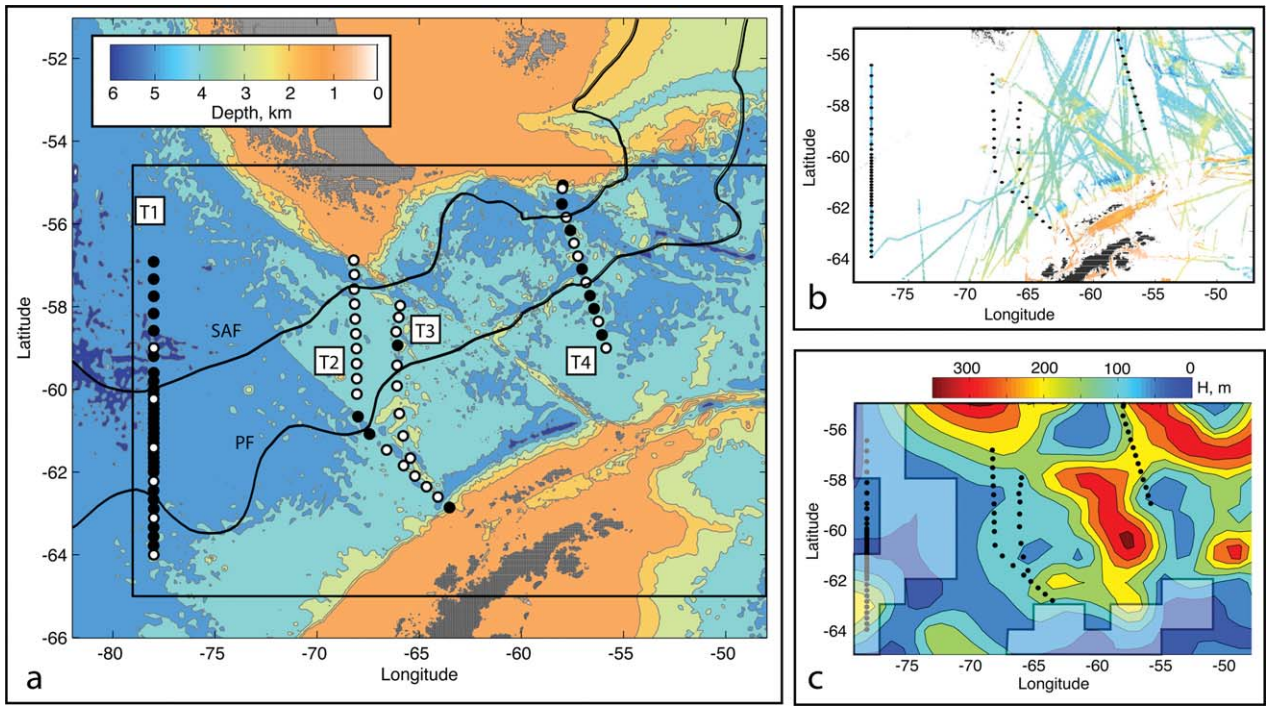

Figure 1. (a) Bathymetry map of the DIMES region of study [*Smith and Sandwell*, 1997]. White circles = microstructure and finestructure profile locations along transects T1, T2, T3, and T4; black circles = finestructure only profiles; solid black lines = position of Subantarctic Front (SAF) and Polar Front (PF) from *Orsi et al*. [1995]; black box = region shown in the remaining subfigures. (b) Multibeam bathymetry data provided by A. Tate, British Antarctic Survey, 2012. Data were provided on a 0.002° grid. Black circles = profile locations as in Figure 1a. (c) Contour plot of the square root of topographic height variance, H, derived from spectral analysis of multibeam data in Figure 1b. Black circles = profile locations as in Figure 1a; transparent boxes indicate regions where data limitations meant that fewer than two spectra were analyzed.

$\epsilon_{\text{micro}} = 15\nu/2\ \overline{(\partial u/\partial z)^2}$, where ν is the molecular viscosity [*Oakey*, 1982].

[8] Three microstructure profiling instruments were used during the DIMES survey: the High-Resolution Profiler 2 (HRP2), built at the Woods Hole Oceanographic Institution (WHOI), and two Rockland Scientific International VMP-5500 instruments (http://www.rocklandscienticfic.com). HRP2 is similar to the original HRP, as described by *Schmitt et al*. [1988]. Availability of at least two instruments on each cruise allowed near-continuous sampling. Careful comparison of processing routines and instrument noise was carried out to ensure no systematic bias between the various instruments. Processing was conducted using algorithms developed originally for the HRP [*Polzin and Montgomery*, 1996; *Naveira Garabato*, 2009]. For VMP data, velocity shear variances were computed every 0.5 dbar, using bin widths of 1 s, with a sampling rate of 512 Hz. Computed dissipation rates were subsequently interpolated onto a 2 dbar grid. Each instrument carried two shear probes, and unless one was deemed particularly noisy, the mean of the dissipation estimates from the two probes was used. The diapycnal diffusivity, K_ρ, was computed using the Osborn relation, $K_\rho = \Gamma\epsilon_{\text{micro}}/N^2$, where N is the buoyancy frequency, and Γ is the mixing efficiency parameter, taken to be 0.2 [*Osborn*, 1980; *Oakey*, 1982]. At most stations, data were collected to within 100 m of the sea floor. Microstructure cast locations were recorded as the midpoint between the instrument deployment and recovery position (profiler drift was rarely more than a few kilometers).

2.3. Finestructure

[9] To characterize the internal wavefield, finescale measurements of temperature, pressure, salinity, and current velocity were obtained from conductivity temperature depth (CTD) and lowered acoustic Doppler current profiler (LADCP) measurements. These instruments have vertical resolutions of $O(1\text{ m})$ and $O(10\text{ m})$, respectively, capturing internal wave scales. The CTDs employed were Sea-Bird 911plus, calibrated using water samples collected on sampling rosettes with 24 bottles. Bottle salts were analyzed on Guildline 8400B salinometers, standardized using International Association for the Physical Sciences of the Oceans (IAPSO) P-series standard seawater. Bottle and sensor salinity data were found to agree within ± 0.002. The quoted accuracy of the Sea-Bird 911plus temperature sensor is 0.0005°C (http://www.seabird.com). The LADCP system, comprising two 300 kHz Teledyne RDI ADCPs (one downward looking and one upward looking), was mounted on the CTD frame. The LADCPs were programmed to obtain beam-coordinate velocities in 8 m bins. Blanking distance was set to zero but data from the first bin were not used for processing. In section T3, the upward looking LADCP was

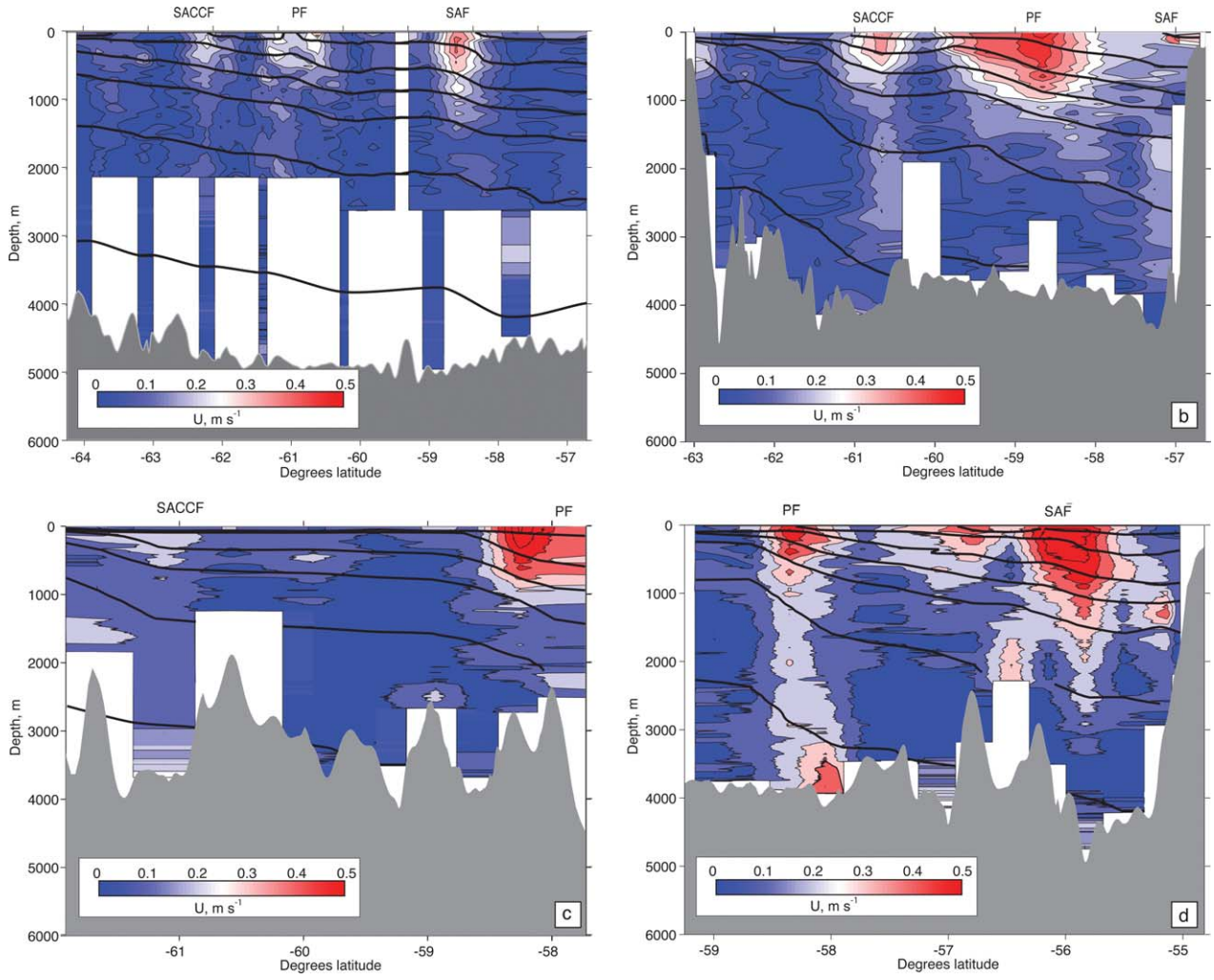

Figure 2. (a–d) Vertical distribution of current speed, U, from LADCP measurements across transects T1, T2, T3, and T4, respectively. Speeds are plotted as shaded contour plots, spaced by 0.05 ms^{-1}. Thick black lines = 0.2 kg m^{-3} neutral density contours. Positions of the Southern Antarctic Circumpolar Current Front (SACCF), PF, and SAF are indicated on the top axis. Note some stations are not full depth.

misprogrammed and the corresponding data were discarded. Thus, for consistency, only data from the downward looking instrument were used for all sections. Horizontal velocities and their corresponding vertical shears were obtained from the CTD/LADCP data using the velocity-inversion method [*Visbeck*, 2002]. Vertical shear was calculated separately for the downcast and upcast profiles. To obtain absolute velocity profiles, the downcast and upcast data were combined and velocity referencing was accomplished using bottom-track data, shipboard-ADCP, and vessel global positioning system (GPS) information. At stations where both finestructure and microstructure data were obtained, CTD and LADCP casts were conducted between VMP/HRP2 deployment and recovery.

[10] The finestructure data are used to compute the variation of four parameters:

[11] (1) Indirect estimates of turbulent dissipation, ϵ_{fine}, computed by comparing measured shear (i.e., the vertical gradient of the horizontal velocity) and strain (i.e., the vertical gradient of vertical displacement of isopycnals) spectra with the Garrett-Munk (GM) model predictions and utilizing wave-wave interaction parameterizations, such as outlined by *Henyey et al*. [1986], *Gregg* [2003], and *Polzin et al*. [1995]. The method assumes a cascade of energy, driven by nonlinear wave-wave interactions, from vertical internal wave scales (10–100 m) to dissipative small-scale turbulent motions. We note that the validity of wave-wave parameterizations may break down under several conditions, such as near boundaries (K. L. Polzin et al., Finescale parameterizations of turbulent dissipation, in preparation, 2012, hereinafter referred to as Polzin et al., in preparation, 2012). In most cases, both shear and strain spectra were computed over depth bins of 512 m and analyzed between vertical wavelengths of 60–180 m, encompassing internal wave scales. Vertical wavelength bounds are limited by spectral drop off at lower wave numbers, noise at high wave numbers and limitations to analyzing depth variability within each profile if spectra are computed over too wide a depth range. We find dissipation patterns are generally robust to varying shear and strain wavelength integration ranges between 60 and 320 m (see Appendix A1 for more details).

[12] (2) Internal wave energy, E_{IW}, computed as the sum of horizontal kinetic energy and potential energy. As for shear and strain spectra, energy spectra were computed for 512 m depth bins and integrated over a 60–180 m vertical wavelength band.

[13] (3) Shear-to-strain ratio, R_ω, which provides information on the frequency content of the internal wavefield. For a single wave, $R_\omega \cong (\omega^2 + f^2)/(\omega^2 - f^2)$. The GM value for R_ω is 3. Lower values of R_ω indicate a preponderance of higher frequency internal waves, whereas enhanced R_ω values are associated with a more near-inertial internal wavefield.

[14] (4) The dominant vertical direction of internal wave energy propagation, determined using the ratio of counterclockwise polarized shear variance (CCW) to clockwise polarized shear variance (CW) i.e., the polarization ratio, $R_{pol} = \mathrm{CCW}/\mathrm{CW}$ [*Gonella*, 1972]. In the Southern Hemisphere, a predominance of downward energy propagation is associated with a dominance of counterclockwise shear variance, i.e., when $R_{pol} > 1$.

[15] Further details on computing the above internal wavefield parameters are given in Appendices A1 and A2.

2.4. Topography and Lee-Wave Radiation

[16] Following *Goff and Jordan* [1988], three parameters are used to characterize the small-scale topography in the DIMES region: H^2, the variance of the topographic height; k_o, the characteristic wavenumber of topographic variation; and μ, which determines the transition from internal-wave-generating abyssal hills to large-scale topographic features. We derive these parameters using topographic height spectra from multibeam bathymetry (Figure 1b). To fully capture the anisotropy of topographic undulations, which are generally aligned northwest to southeast across Drake Passage, and the effect of the varying direction of the deep geostrophic flow, two-dimensional topography spectra are required. However, we are limited by the areal coverage of multibeam bathymetry data. (Other available topography data, such as that from *Smith and Sandwell* [1997], do not capture the small scale abyssal hills (1–10 km) that are most effective at generating lee waves). We instead split the available multibeam data into overlapping 2° latitude × 4° longitude boxes and synthesize single-track topography data in eight different directions within each box. The topographic parameters, H^2, k_o, and μ, for each box-mean track direction were determined by fitting the observed spectra to that of the Goff and Jordan model spectrum in log-log space [*Goff and Jordan*, 1988; *Nikurashin and Ferrari*, 2011, 2010b]. Further details are provided in Appendix B.

[17] The rate of lee-wave energy radiation, E_r, induced by bottom flows impinging on topographic features may be predicted using linear-wave radiation theory, as first described by *Bell* [1975]:

$$E_r = \rho_o U_o \int_{k_{x1}}^{k_{x2}} P_{\mathrm{eff}} \sqrt{\left(N_o^2 - U_o^2 k_x^2\right)} \sqrt{\left(U_o^2 k_x^2 - f^2\right)} \mathrm{d}k_x, \quad (1)$$

where f, N_o, U_o, and ρ_o are the Coriolis parameter, the bottom stratification, the bottom current speed, and the density, respectively. The value of k_x is the radiated horizontal wavelength (cyc m^{-1}) and $P_{\mathrm{eff}} = H^2 k_o^{\mu-2}(\mu-2)k_x^{-(\mu-1)}\beta[0.5, (\mu-1)/2]$ [*Nikurashin and Ferrari*, 2010b]. The values k_{x1} and k_{x2} indicate the range of horizontal wavelengths that may be generated, such that $k_{x1} = f/U_o < k_x < N_o/U_o = k_{x2}$. N_o and U_o were determined as the observed mean values within 500 m of the seabed, as in *Nikurashin and Ferrari* [2011]. For each station, we choose the closest computed topographic parameters (unless they are more than 4° away), associated with the spectral tracking direction corresponding to the station mean bottom flow direction. Maximum and minimum energy fluxes for varying flow directions were also computed.

[18] The saturation of radiated lee-wave energy at supercritical topography is accounted for by the steepness parameter, $S = N\sqrt{2}H_{\mathrm{rms}}/U_o$, where H_{rms} is the rms height of topography in the radiative wavenumber range [*Nikurashin and Ferrari*, 2011]. For topographic steepness greater than 0.7, E_r is multiplied by $(0.7/S)^2$ to represent the effect of saturation.

3. Observations

3.1. Microstructure

[19] Mid-depth dissipation rates are found to increase from $O\left(1 \times 10^{-10}\ \mathrm{W\ kg^{-1}}\right)$ in the southeast Pacific sector to $O\left(1 \times 10^{-9}\ \mathrm{W\ kg^{-1}}\right)$ in the Scotia Sea (Figures 3 and 4a–4d). Translating these to diapycnal diffusivities gives values of K_ρ of $O\left(1 \times 10^{-5}\ \mathrm{m^2\ s^{-1}}\right)$ and $O\left(1 \times 10^{-4}\ \mathrm{m^2\ s^{-1}}\right)$, respectively (Figures 4e–4h). For all transect mean profiles, turbulent dissipation rates are greatest near the seabed, reaching $3 \times 10^{-9}\ \mathrm{W\ kg^{-1}}$ (or a diapycnal diffusivity of $1 \times 10^{-3}\ \mathrm{m^2\ s^{-1}}$) in transects T2 and T3. Bottom enhancement is confined to within ~1 km of the seabed on transects T1 and T2, but reaches up to 2 km above the bottom on the Phoenix Ridge transect. At T4, dissipation values remain close to near-bottom values throughout the water column. Along transects T1 and T4, interstation variability in turbulent dissipation is relatively small, whereas significant variability is exhibited on both the western Drake Passage (T2) and Phoenix Ridge (T3) transects. Typically, stations with higher turbulent dissipations, particularly in the bottom kilometer, are concentrated at and to the north of the Polar Front (PF). For example, the single station located to the south of the PF on transect T4, at 59°S, has dissipation rates 10 times lower than those found north of the front (Figure 3d).

[20] Enhancement of dissipation within frontal zones of the ACC was previously identified by *St. Laurent et al.* [2012] in both the western Drake Passage and the Phoenix Ridge transects. This pattern was cited as a key indication that deep-reaching ACC jets provide energy for the observed near-bottom turbulence, through encountering rough topography. Here, we find further evidence to support this hypothesis. Higher turbulent dissipation rates across all transects are clearly associated with regions of higher current speeds and rougher topography (Figure 5). This relationship also hints that the generation of internal waves by subinertial flows impinging on topography dominates over tidally generated internal waves in the ACC (Brearley et al., submitted manuscript, 2013). In the next section, we carry out a more detailed analysis of the

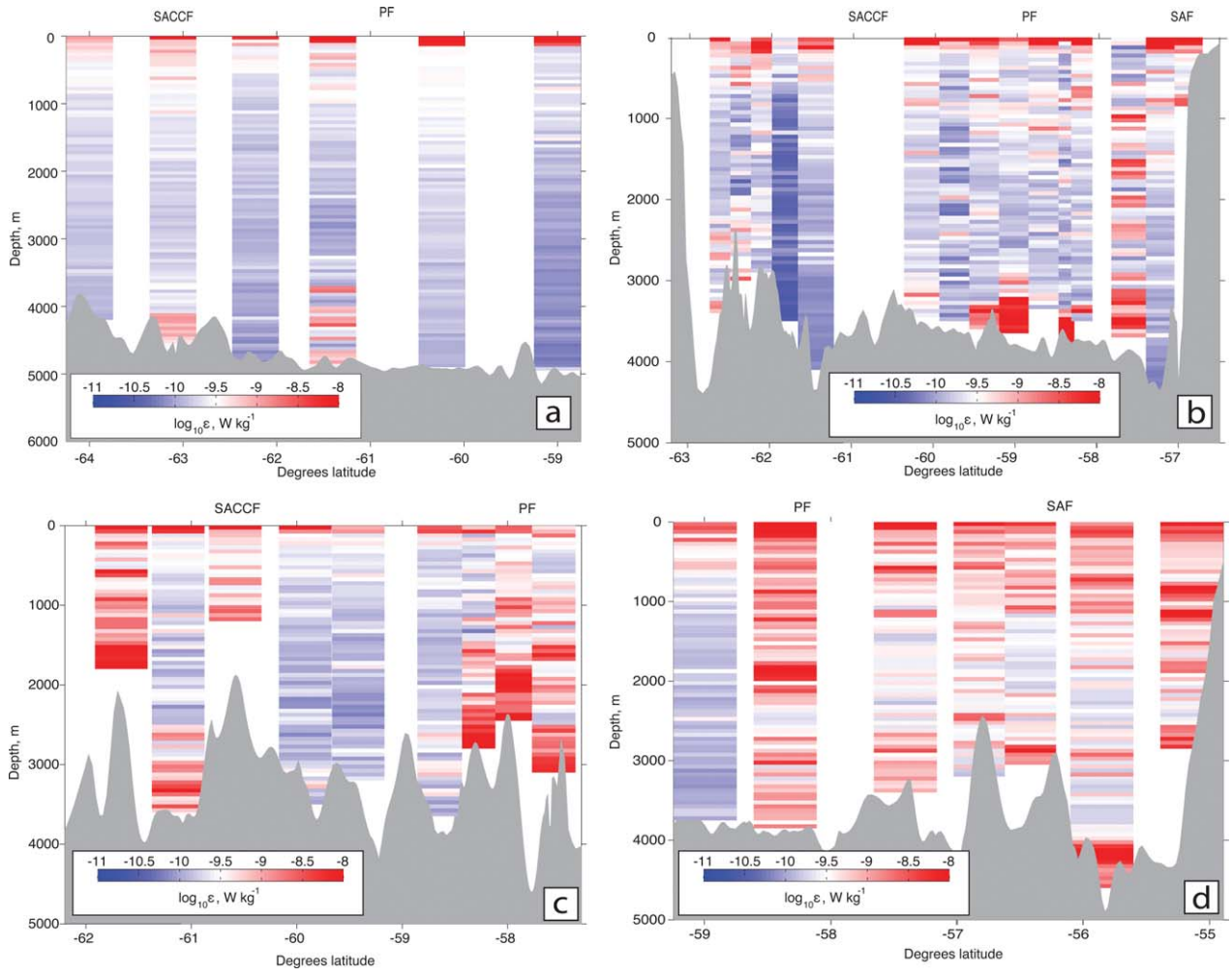

Figure 3. (a–d) Vertical profiles of turbulent energy dissipation, ϵ_{micro}, from VMP and HRP2 measurements across transects T1, T2, T3, and T4, respectively. Note the different horizontal scale between Figure 3a and Figures 2a and 6a.

internal wavefield in order to uncover the physical processes underpinning these observations.

3.2. Finestructure

[21] Analysis of internal wavefield characteristic parameters, as described in section 2.3, supports the hypothesis that abyssal turbulent dissipation is mediated by breaking internal lee waves. First, we find that the spatial pattern of finestructure-deduced dissipation rates closely matches that derived from microstructure and that internal wave energy is clearly seen to increase with increasing energy dissipation (Figures 3, 6, and 7). This relationship suggests that small-scale turbulent overturning within the DIMES region is largely powered by energy from the internal wavefield. Note the systematic overprediction of finestructure-derived dissipation rates to microstructure estimates, suggesting a departure from the physics of wave-wave interaction processes. This observation is discussed further in section 5.3.

[22] Second, we examine the frequency content of the internal wavefield. Mid-depth shear-to-strain variance ratios, R_ω, in the eastern Pacific transect (T1) are typically ~10, but gradually reduce to ~5 in the easternmost transects, T3 and T4 (Figure 8). The wavefield downstream of Drake Passage, where higher dissipation rates are measured, is thus less inertial than in the southeast Pacific. A significant negative correlation is found between R_ω and microstructure-deduced dissipation rates (Figure 9) highlighted, for example, by a qualitative comparison of Figures 3b and 8b. This observation is consistent with an enhancement of bottom-generated lee waves, over wind-generated near-inertial internal waves, downstream of Drake Passage. The lowest values of R_ω, and hence least inertial internal waves, are found in the bottom kilometer of transects T2 and T3, where the greatest bottom enhancement of turbulent dissipation is observed.

[23] Third, we consider the dominant direction of internal wave energy propagation, using rotary shear spectra (Figure 10). Although the distribution of the polarization coefficient is rather noisy, probably reflecting the relatively short depth bin of 512 m over which the shear spectra were computed, some patterns are discernible. In the upper ocean, areas of dominant downward energy propagation are found at frontal regions, in particular the PF (e.g., stations between 60.5°–61.5°W in transect T1, stations at

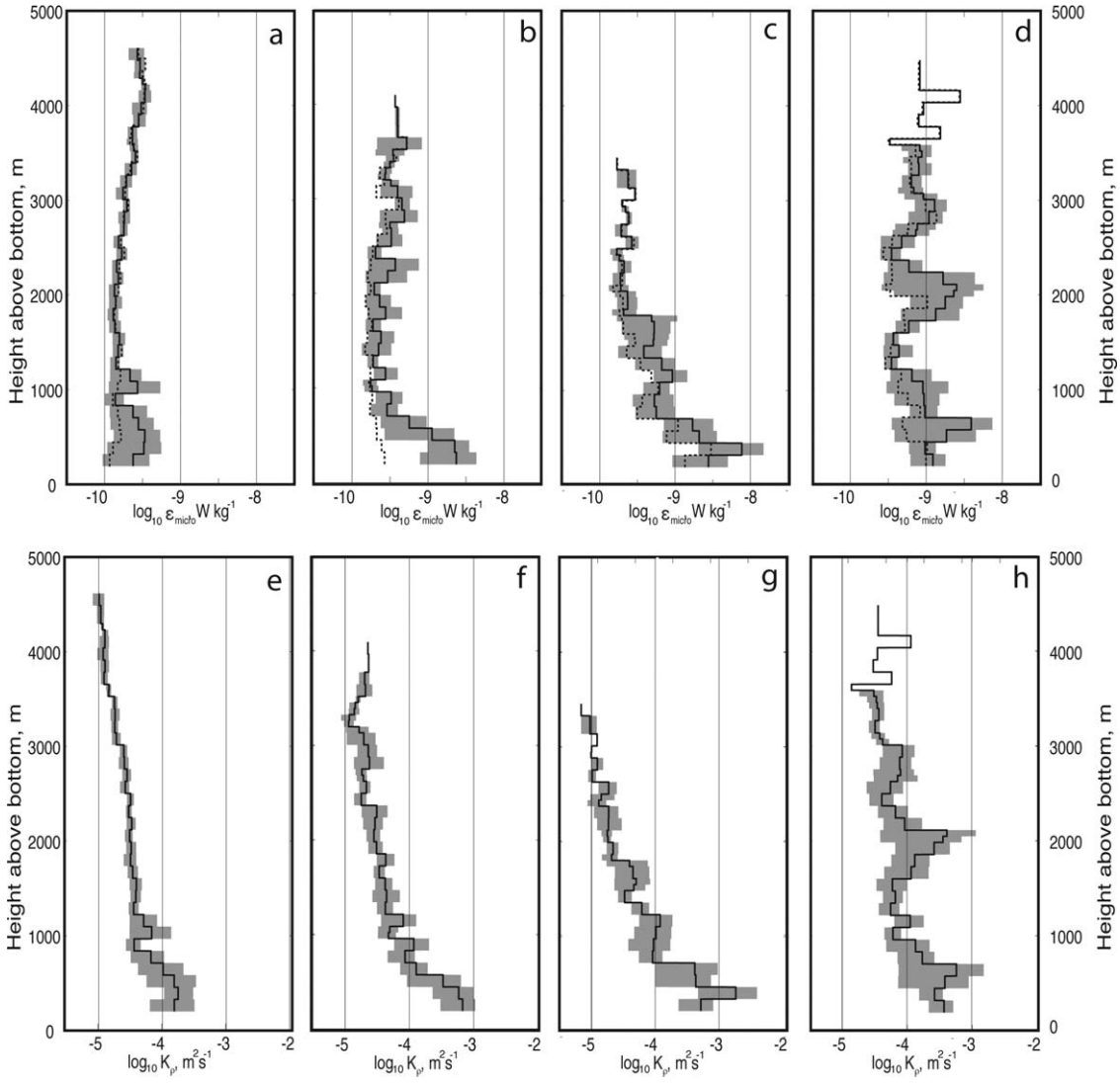

Figure 4. (a–d) Mean (solid) and median (dashed) dissipation values across the profiles as a function of height above bottom, for transects T1, T2, T3, and T4. Data are averaged into depth bins corresponding to finestructure spectral analysis bins. Shaded regions mark the 90% confidence interval in mean values, calculated by bootstrapping. (e–h) Mean transect diapycnal diffusivity, K_ρ, as a function of height above bottom, for transects T1, T2, T3, and T4.

58°–59°W in transect T2 and stations at 58°–58.5°W in transect T3). This observation may be attributed to strong wind work at frontal regions, forcing more downward propagating waves [e.g., *Alford*, 2003]. Alternatively, background shear associated with frontal jets may modulate near-inertial wave propagation. *Kunze* [1985] report that downward-propagating near-inertial waves may be trapped and amplified in frontal regions.

[24] In transect T4, where enhanced dissipation is observed throughout the water column, upward propagating internal wave energy dominates at all depths. In addition, polarization ratios clearly decrease eastward through Drake Passage. To determine whether this change is caused by a decrease in downward directed energy or an increase in upward propagating energy, it is useful to consider transect-mean counterclockwise and clockwise shear variances independently. We find that the strong polarization signal observed in the upper 2000 m or so of the Pacific sector is due to less upward propagating energy (as opposed to more downward propagating energy), relative to the transects east of Drake Passage. We thus conclude that differences in the prevalent direction of vertical energy propagation within the DIMES region are dominated by variability in the radiation of bottom-generated internal waves as opposed to wind-driven internal waves sourced at the sea surface. Although all the high dissipation values fall within regions of dominant upward energy propagation, we do not find a significant correlation between dissipation rates and polarization ratio, which is likely due to the rather noisy nature of the polarization coefficient.

[25] In summary, we find that regions of high dissipation, found most prominently in the lower kilometer of transects T2–T4, are associated with enhanced internal wave energy with a preponderance of upward energy flux

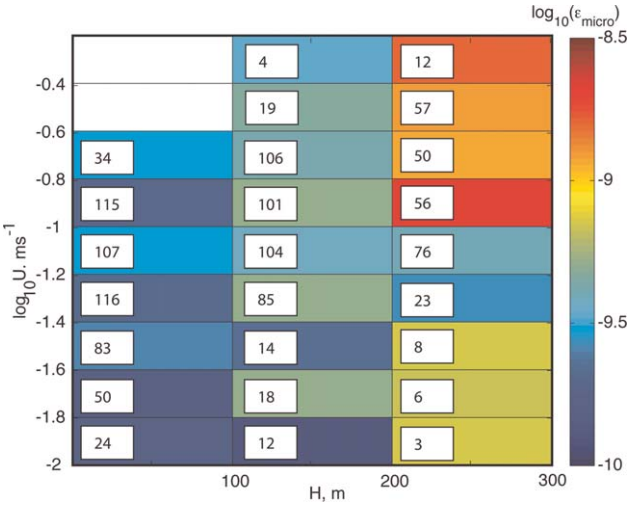

Figure 5. Distribution of turbulent dissipation, as a function of bottom roughness, *H*, and current speed, *U*. Dissipation values represent the mean values over finestructure spectral depth bins for the full water column. Labeled numbers show the number of data points in each *H*-*U* bin.

and higher-frequency motions. In contrast, regions with polarization ratios greater than 1, which are concentrated in the southeast Pacific and in the upper water column, are characterized by lower-frequency, near-inertial waves, consistent with wind forcing being the dominant source of finescale variance and in turn turbulent kinetic energy dissipation. These observations lend support to the hypothesis that bottom-generated lee waves play a major role in transferring energy from the subinertial flow to turbulent dissipation and diapycnal mixing. In the next section, we assess the consistency of the observed turbulent dissipation and internal wave energy across the DIMES region, with current theoretical ideas concerning lee-wave generation.

4. Lee-Wave Radiation by Geostrophic Flow Over Topography

[26] The energy flux from bottom-generated lee waves may be computed using modified linear theory, as described in section 2.4. Equation (1) shows that predicted lee-wave energy fluxes are largely dependent on the bottom flow and stratification, alongside the characteristics of the local topography. The distribution of topographic height

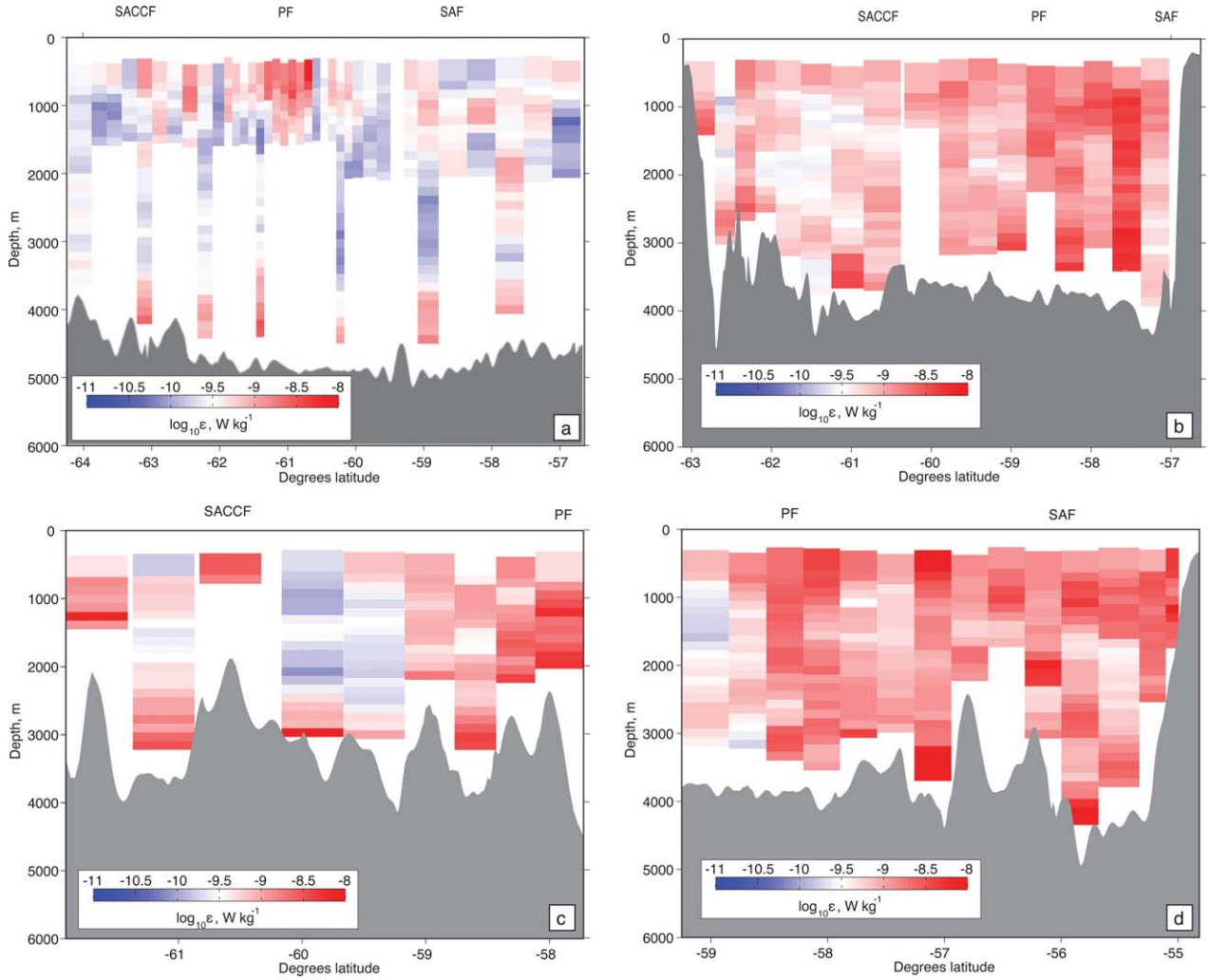

Figure 6. (a–d) Vertical distribution of finestructure-deduced dissipation rates, ϵ_{fine}, across transects T1, T2, T3, and T4, respectively. The uppermost 200 m or so of data are missing, as shear and strain spectral bins are computed starting from the bottom of the CTD/LADCP cast.

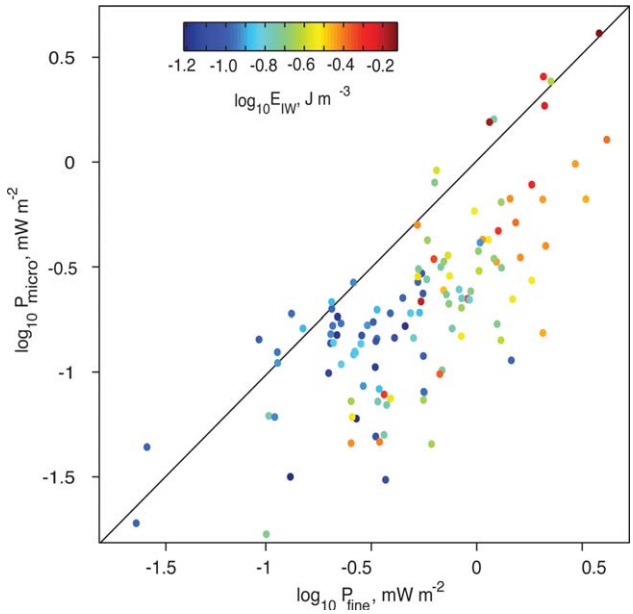

Figure 7. Scatter plot of microstructure-deduced dissipation power versus finestructure estimates. Power is computed by multiplying turbulent dissipation rates by density and depth integrating over 1 km bins. Values shown encompass the full depth of each profile. The density field is estimated from CTD measurements. Correlation coefficient = 0.73. Circle colours = mean internal wave energy in corresponding depth bin. E_{IW} is computed as described in Appendix A2. Diagonal black line = one to one relationship.

variance, H^2, across the DIMES region, computed using multibeam bathymetry data (section 2.4), bears a close qualitative resemblance to the large-scale bathymetry (Figures 1a and 1c). The square root of the topographic height variance increases from 30 m in the southeast Pacific to 210 m along T4. H reaches a maximum (∼300 m), along the topographic ridge east of T3. We acknowledge that a lack of data along the northern half of the Phoenix Ridge may bias values low here. For comparison, *Nikurashin and Ferrari* [2010b] find $H = 305$ m in Drake Passage, whereas our values are typically 100–300 m in western Drake Passage and 100–200 m at the Phoenix ridge.

[27] Along the T1 transect in the Southeast Pacific, predicted internal wave-energy radiation estimates, E_r, are relatively uniform, typically 0.1–1 mW m^{-2} (Figure 11a). In contrast, the western Drake Passage (T2), Phoenix Ridge (T3), and eastern Drake Passage (T4) transects display greater spatial heterogeneity in predicted energy radiation values, chiefly due to greater variation in bottom current speeds. Here, internal wave energy fluxes are generally between 1 and 100 mW m^{-2}, with a maximum of 140 mW m^{-2} at 58°S in T4, a site beneath the PF where strong current velocities reached to the seabed (Figures 2d and 11d). Transect-average values of energy radiation are 0.8, 3.1, 6.9, and 13.6 mW m^{-2}, for transects T1, T2, T3, and T4, respectively (Figure 12). The substantial increase in transect-averaged radiation values with distance downstream along the ACC reflects the increasing topographic roughness and, to a lesser extent, higher bottom velocities found on the eastern transects. The values compare well with those discussed by *Nikurashin and Ferrari* [2010b], who reported lee-wave generation rates of 0.5–3.9 mW m^{-2} in the southeast Pacific and 14–42 mW m^{-2} in western Drake Passage.

[28] We next investigate how turbulent dissipation values and internal wavefield energy estimates compare to internal wave energy flux predictions. Encouragingly, regionally averaged patterns of predicted energy fluxes and turbulent dissipation rates depth-integrated over the bottom kilometer, are similar, and both show a sharp increase between western Drake Passage (T2) and the Phoenix Ridge (T3); Figure 12. This observation supports the role of lee-wave generation in determining the spatial distribution of abyssal ocean mixing. However, the relationship breaks down for the southeast Pacific transect (T1) if full-depth-integrated values of dissipation are used. Here, microstructure-deduced energy dissipation rates are higher than the radiative predictions, which is unsurprising given that wind-generated internal waves were previously argued to be the dominant source of internal wave energy in the southeast Pacific (section 3.2). We also note that the mean-predicted lee-wave flux along T4 is largely skewed by the station at the PF: to highlight this, median values are also plotted in Figure 12. Microstructure-derived abyssal energy dissipation rates, integrated over depths within 1 km of the seabed at which finestructure data are also available, are found to contribute ∼21% of lee-wave energy flux predictions in the southeast Pacific, reducing to ∼7% for the more eastern transects. If depths below which finestructure data were recorded are included, these values increase to 27%, 30%, 26%, and 9% for transect T1,T2, T3, and T4, respectively. Finestructure-derived abyssal values are found to be 79%, 29%, 17%, and 11% of the predicted lee-wave source energy for transects T1, T2, T3, and T4, respectively. These fractions are comparable to those found by Waterman et al. (submitted manuscript, 2012) in the vicinity of the Kerguelen Plateau, although we note that the high abyssal finestructure estimates in T1 are likely a result of the low LADCP signal-to-noise ratio here (see section 5.3). The results indicate that the bulk of the energy associated with turbulent mixing may indeed be sustained by the response of ACC flow to sea-floor topography; however, the reasons for large excess in the predicted radiated energy are unclear. Comparison of microstructure to finestructure-derived dissipation, suggests that a significant proportion of this unaccounted for energy is present in the local internal wavefield, but it appears not to have cascaded down to turbulent scales. This "overprediction" of finescale-deduced dissipation rates over microstructure estimates is examined in section 5.3.

5. Evolution of Bottom-Sourced Internal Waves

5.1. Effect of Deep-Reaching ACC Jets on the Internal Wavefield

[29] Assuming a linear regime, steady flow, and sinusoidal topography, lee-wave vertical wavelengths can be computed as $\lambda_{lee} = 2\pi U_o/N_o$ [*Gill*, 1982]. Using bottom current speed and stratification, averaged over the bottom 500 m, we compute transect-mean lee-wave vertical wavelengths, both inside and outside of jets. A station is defined as being inside a jet when $U_o > U_{o,\mathrm{mean}}$, where $U_{o,\mathrm{mean}}$

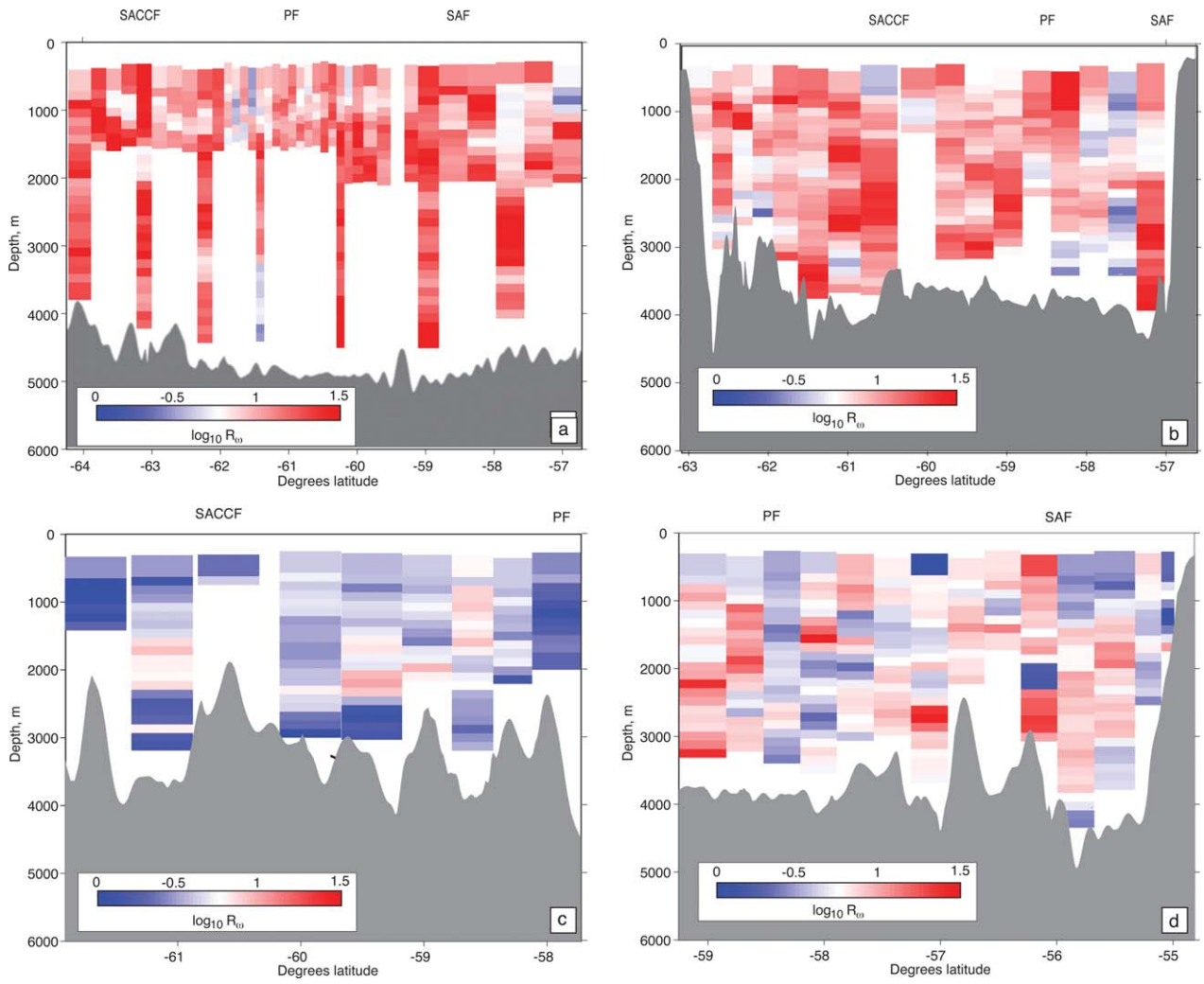

Figure 8. (a–d) Vertical distribution of the shear-to-strain variance ratio, R_ω, across transects T1, T2, T3, and T4, respectively. Higher R_ω values indicate a more inertial wave content.

represents the mean near-bottom speed across the transect. Predicted wavelengths inside jets are 897 ± 190 m, 1122 ± 161 m, 1296 ± 187 m, and 1770 ± 465 m for transects T1, T2, T3 and T4, respectively. Wavelengths outside jets are smaller with mean values of 238 ± 49 m, 548 ± 160 m, 669 ± 177 m, and 524 ± 82 m for the four transects. These wavelength predictions are generally greater than the vertical scales over which we choose to integrate internal wave parameters (60–180 m). Regardless, analysis of strain and shear spectra over depth bins of 2048 m reveals no obvious spectral enhancement at the predicted lee-wave wavelengths. We note that linear lee-wave theory may be an oversimplification, overpredicting wavelengths and wave energy due to the assumption of steady flow, disregard of finite-amplitude topography effects or nonlinear feedback mechanisms. In addition, processes may exist by which energy is transferred from motions with longer vertical wavelengths and more near-inertial frequencies to shorter-wavelength, higher-frequency waves (Brearley et al., submitted manuscript, 2013). In the Phoenix Ridge (T3) and SR1b (T4) transects, internal wave spectral variance at wavelengths between 60 m and 180 m for stations

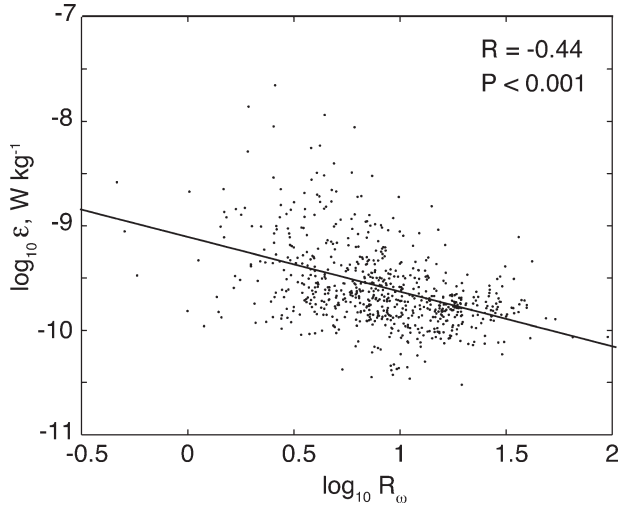

Figure 9. Correlation between the shear-to-strain variance ratio, R_ω, and microstructure-deduced dissipation rates, ϵ_{micro}, for all data. The correlation coefficient, R and p value, P, are indicated.

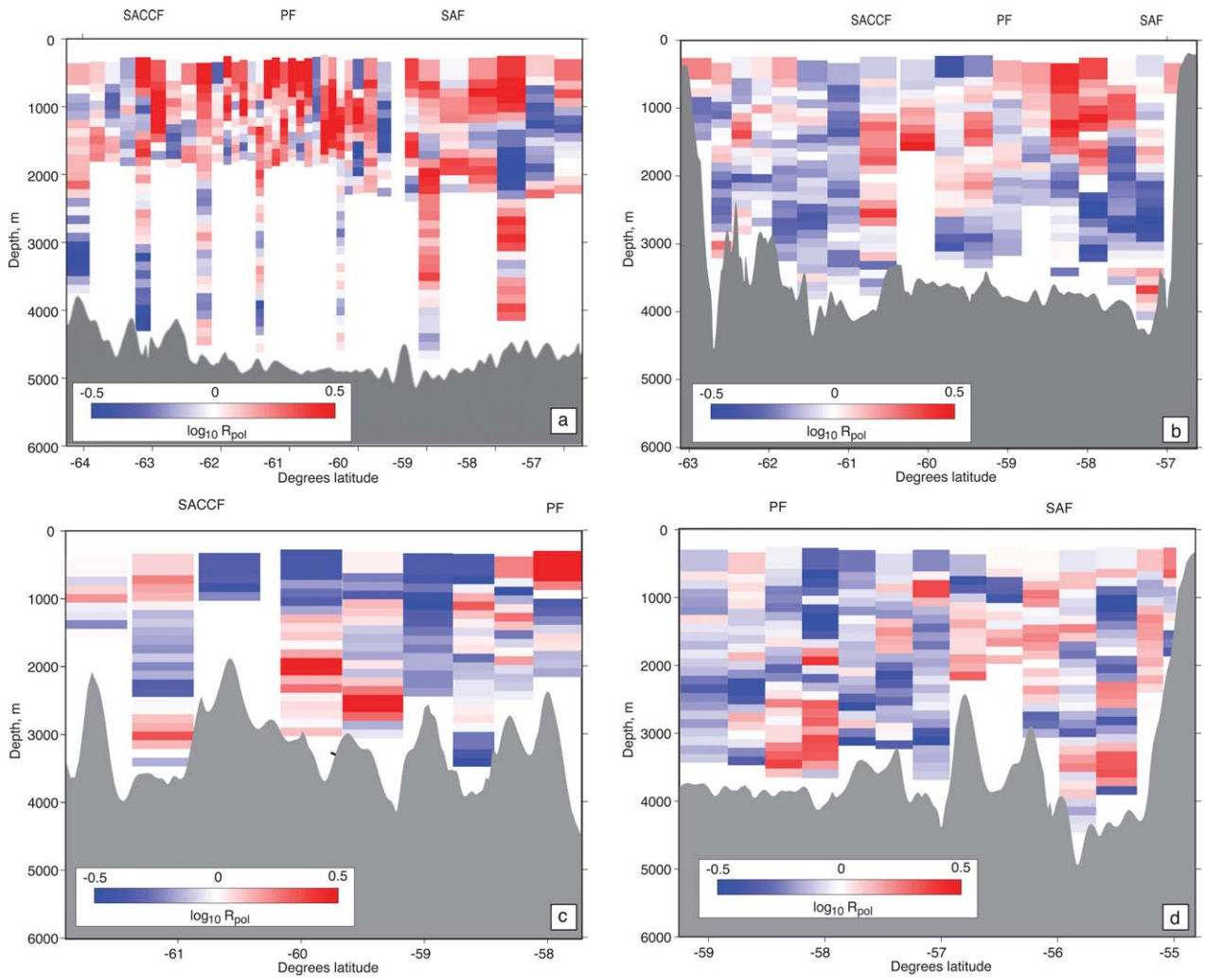

Figure 10. (a–d) Vertical distribution of the polarization ratio, $R_{\mathrm{pol}} = \mathrm{CCW}/\mathrm{CW}$, across transects T1, T2, T3, and T4, respectively. R_{pol} is computed by integrating counterclockwise and clockwise shear spectra from LADCP measurements. $R_{\mathrm{pol}} > 1$ indicates a dominance of downward propagating internal wave energy.

within jets is enhanced (Figure 13). Apart from a small region 1–1.5 km above the sea bed, strain and shear variances inside and outside of jets are found to be statistically different (standard errors do not overlap and a Wilcoxon rank sum test indicates that the distributions have different medians at the 90% confidence level). The frequency content of the internal wavefield is found to be statistically different inside and outside of jets up to 800 m above the seabed. The spectral enhancement within the jets is particularly prevalent in strain data, such that faster bottom flow appears to be related to highly strained, higher-frequency internal waves for vertical wavelengths of $O(100$ m). In the Phoenix Ridge transect (not shown), this region of enhanced strain is found up to 2000 m above the seabed, in accordance with the depths at which enhanced dissipation is encountered (Figure 4c).

5.2. Nonlinear Lee-Wave Radiation

[30] *Nikurashin and Ferrari* [2010a] extended linear lee-wave radiation theory to include the feedback of internally generated waves on the alongstream averaged flow. Using numerical simulations, they find that vigorous inertial oscillations are driven near the ocean floor by waves generated at steep topography, which in turn promote wave breaking and turbulent dissipation. Three different regimes of internal wave radiation and dissipation were considered, distinguished by the steepness parameter, $S = N\sqrt{2}H_{\mathrm{rms}}/U_o$. In regions of smoother topography, where $S < 0.3$, classic lee-wave radiation theory was shown to apply, and only 10% of internal wave energy was found to be dissipated locally. As S increases above 0.3, more internal wave energy is radiated and bottom-sourced waves become time dependent, with vigorous inertial oscillations and wave breaking. In this regime, typically 50% of the radiated energy is dissipated in the bottom 1 km. For $S > 0.7$, some fraction of the flow is blocked by topography and the energy flux saturates.

[31] The vertical profiles of turbulent dissipation are generally consistent with these theoretical predictions. The southeast Pacific (T1) dissipation profile is comparatively uniform with depth, in accordance with both smoother topography and low steepness parameters that place it in the

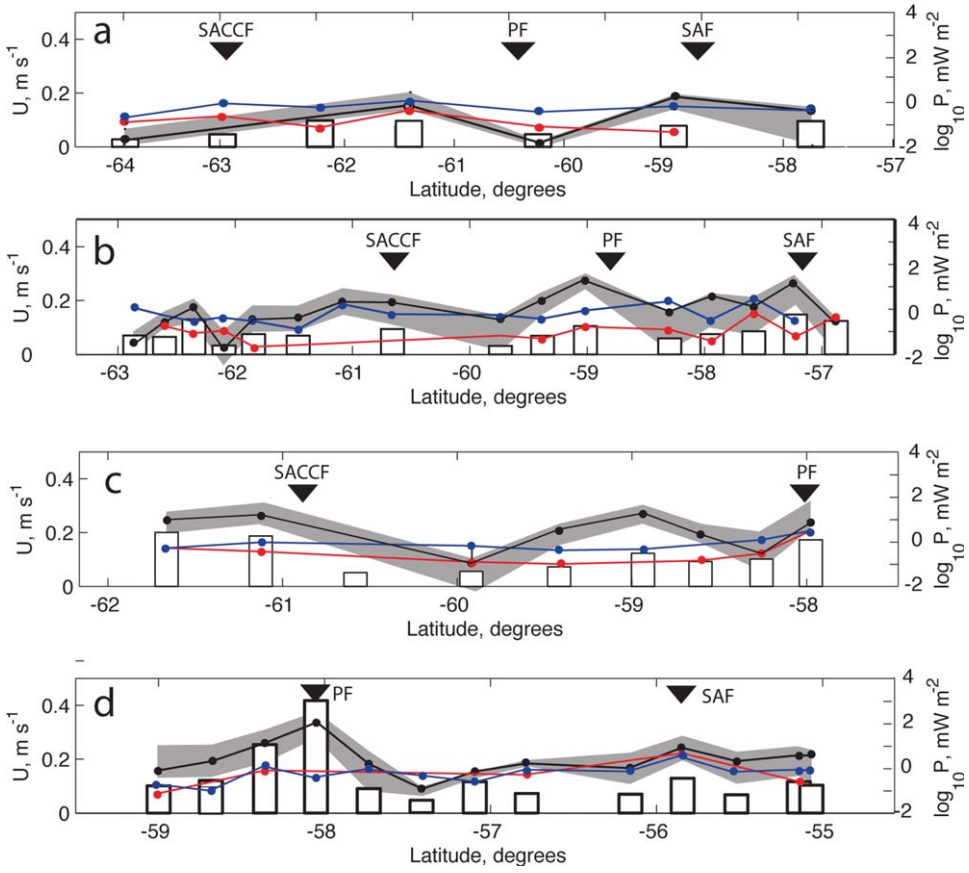

Figure 11. (a) Dots and lines represent the dissipated power per unit area as a function of station latitude along transect T1. Red = mean power in bottom 1 km from microstructure measurements; blue = mean power in bottom 1 km from finestructure-derived turbulent dissipations; black = radiated power computed from linear radiation theory, where shaded regions mark maxima and minima for various current directions; white bars = mean speed 1 km above bottom; black triangles = approximate position of ACC fronts. (b–d) As for Figure 11a but for transects T2, T3, and T4, respectively.

quasi-stationary lee-wave regime (Figure 4a). Here, 26% of the dissipated energy is found within the bottom 1 km (excluding the top 500 m). In contrast, the Phoenix Ridge transect (T3), where steepness values are greater than 0.3 for every station but one, exhibits a marked enhancement of turbulent dissipation in the bottom 1–2 km (Figure 4c), with 76% of energy dissipation in the bottom 1 km. The theory attributes this signal to the presence of inertial oscillations promoting wave breaking in the bottom 1 km. The western Drake Passage (T2) and eastern Drake Passage (T4) transects contain stations that fall into both the linear $(S < 0.3)$ and inertial oscillation $(S > 0.3)$ regimes. Here we find that 63% (T2) and 40% (T4) of energy is dissipated within the bottom 1 km. The smaller steepness parameters in T4 are found in the southern half of the transect and result from reduced bottom stratification and increased bottom velocities, as opposed to smoother topography. By grouping stations according to their steepness parameter, we find that increased dissipation rates within 750 m of the seabed are associated with the inertial oscillation regime (Figure 14). These results are thus consistent with nonlinear theory developed by *Nikurashin and Ferrari* [2010a], and may explain the high level of turbulent dissipation observed throughout the water column in transect T4.

5.3. Finescale Overprediction of Turbulent Dissipation

[32] Earlier analysis of turbulent dissipation rates indicated a notable overprediction by the finestructure parameterizations in some regions (sections 3.2 and 4). Finescale predictions of dissipation values are found to exceed those from microstructure by factors up to 8 in the bottom 500 m of transects T1, T2, and T3, but are more typically twice as large as the microstructure-derived values (Figure 15). We believe that the overprediction signal in the lowly stratified region near the seabed in T1, is a reflection of low LADCP signal-to-noise ratio: there is no clear distinction between averaged counterclockwise and clockwise rotary shear spectra at wavelengths below 150 m and the shear spectra here appear more noisy (Figure 16e). We therefore choose to exclude data in T1 within 2 km of the seabed from the discussion in the remainder this section.

[33] Several reasons lead us to believe that the observed overprediction in transects T2–T4 is not simply a reflection of intrinsic parameterization biases and may provide insights into the underlying physics of the ACC.

[34] First, because there is a strong overprediction signal at all depths in western Drake Passage (T2) and along the Phoenix Ridge (T3), we discount overprediction as being

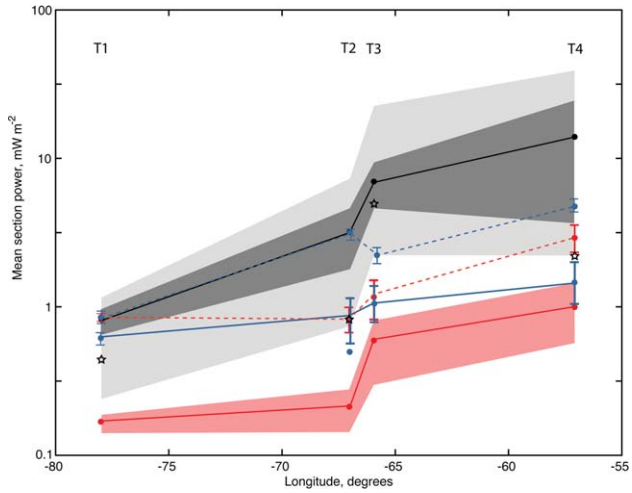

Figure 12. Solid black line = transect-averaged predicted lee-wave energy radiation flux, E_r, against mean transect longitude; light gray shading represents maxima and minima for different current flow directions; black stars = median values of E_r; solid red line = transect mean dissipated power within 1 km of the seabed, estimated from microstructure measurements at depths where coincident finestructure data was available; dashed red line = mean transect power dissipated in entire water column, excluding top 500 m, from microstructure estimates; solid blue line = mean transect power dissipated in the bottom 1 km from finestructure measurements; dashed blue line = mean transect finestructure-deduced power dissipated across the entire water column; error bars and shaded regions mark the standard error in the mean.

due to a manifestation of higher LADCP noise at greater depths or near-boundary interactions in these regions (Figure 15). Furthermore, the enhanced spectral energy at overprediction sites is strongest in strain (not shear) spectra at wavelengths of ~100 m and confined to wavelength bands not associated with spectral noise (Figure 16). This enhanced strain variance at 100 m wavelengths is not apparent in regions of overprediction in T1, supporting our previous concerns over the deep shear data here.

[35] Second, we can qualitatively relate the distribution of finestructure overprediction with other internal wavefield characteristics. Most of the overprediction occurs in regions of higher frequency internal waves and, to a lesser extent, where clockwise shear (i.e., upward propagating energy) dominates. For example, finestructure and microstructure turbulent dissipation rates match well in the southeast Pacific at depths above 1.5 km from the bottom, where the wavefield is more inertial ($\omega < 1.25f$) and dominated by downward propagating energy. Despite this qualitative observation, we do not find a significant correlation between finescale overprediction and shear-to-strain variance or polarization ratio. In section 5.1, we showed that deep-reaching ACC jets are sites of enhanced abyssal shear and strain variances at O(100 m) vertical wavelengths. Such spectral energy signals also appear to be related to regions of finescale overprediction. Transect-mean strain and shear spectra were grouped according to the magnitude of finescale overprediction, and normalized to GM, to elucidate differences in spectral shape (Figure 16). Enhanced spectral variance, in the wavelength band over which internal wave parameters are integrated, is apparent in the regions of finescale overprediction. In addition, qualitative comparison of Figures 2, 3, and 6 indicates that finescale overprediction is most evident at mid-depths beneath the PF in the northern half of T2 and T3.

[36] Waterman et al. (submitted manuscript, 2012) also report finescale overprediction on the Kerguelen Plateau, with a noted enhancement in the bottom kilometer and associated with regions of enhanced dissipation, strong bottom flow, and higher-frequency, upward propagating internal waves. We limit our analysis to the comparison of spatial patterns between the two studies since Waterman et al. (submitted manuscript, 2012) use the "shear-method" to process LADCP data, as opposed to the velocity-inversion method used here [*Thurnherr*, 2012]. Shear-method processed LADCP data are thought to yield slightly higher dissipation estimates than corresponding velocity-inversion estimates. There are competing explanations for the observed finescale overprediction, which Waterman et al. (submitted manuscript, 2012) consider in detail. In light of the new data presented in this study, a few of these ideas are explored below.

[37] We consider the proximity of integration limits to the wave-breaking regime or "critical wavenumber," m_c, defined by $\int_0^{m_c} S[V/N]\mathrm{d}k_z = 2\pi N^2/10$. For $m > m_c$, finescale parameterization theory, based on wave-wave interactions is not expected to apply. We examine the effect of the proximity of the LADCP shear spectral integration range to m_c using HRP2-measured current velocities, which are available for the Phoenix Ridge transect. The greater vertical resolution of HRP2 current velocities (nominally sampled every 0.065 m and averaged over 1dbar bins, compared to the 50 m resolution/8 dbar bins of the LADCP measurements) and reduced noise levels, enable HRP2-deduced shear spectra to be evaluated to m_c in most cases. To extract dissipation estimates from HRP2 finescale data, HRP2 current velocity data were processed identically to the LADCP data but with shear spectra integrated over the wavelength domain 180 m – $1/m_c$, with m_c computed for each depth-binned shear spectra. Figure 15c displays transect mean finescale overprediction values from HRP2 data, which, other than the uppermost bin, fall within the 90% confidence band of LADCP results. Results are also displayed in Tables 1 and 2. We note that the presence of some spurious HRP2 shear variance at wavelengths ~50 m due to instrument spin may bias results a little high. In these data, m_c was found to range from 3 to 30 m, such that the LADCP shear spectral integration limits of 60–180 m are unlikely to encroach on the wave-breaking regime.

[38] We next consider the influence of internal wave interactions with the background flow field on the accuracy of the *Henyey et al.* [1986] finescale parameterizations, which are based on wave-wave interaction physics only. Wave-mean flow interactions may remove energy from the internal wavefield before it has had a chance to dissipate locally, resulting in finescale overprediction (Waterman et al., submitted manuscript, 2012). The Froude number of the background subinertial flow, ($F_r = \sqrt{\overline{U_z}^2/N^2}$), may be

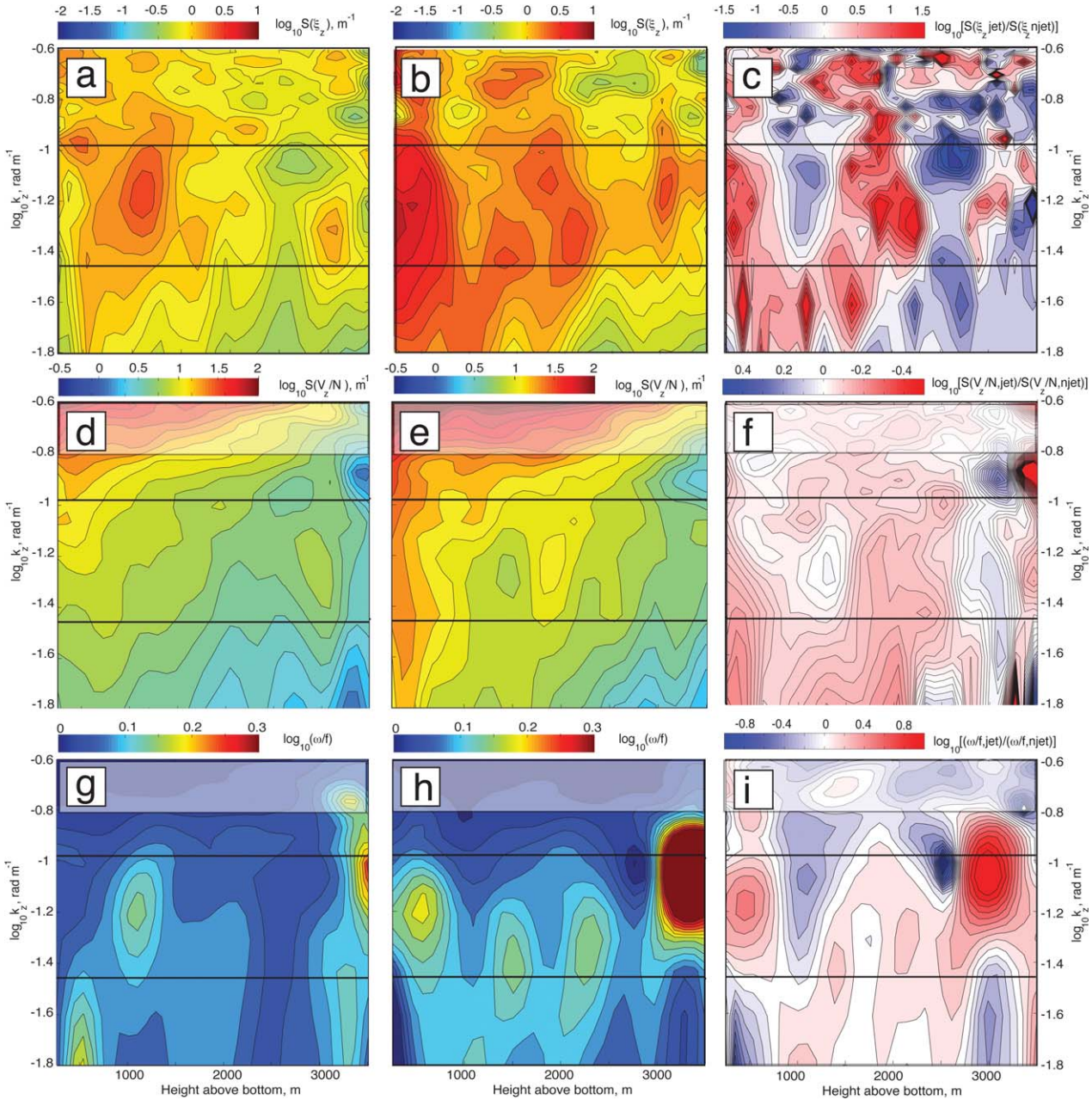

Figure 13. Panels show contour plots of (a and b) strain variance, (d and e) normalized shear variance and frequency content, (g and h) ω/f, in height above bottom, vertical wavenumber space. Figures 13a, 13d, and 13g show mean spectral variances for stations in transect T4 which are found outside of deep reaching jets. Figures 13b, 13e, and 13h show mean of T4 stations within jets. Figures 13c, 13f, and 13i display the ratio of strain variance, shear variance, and frequency content, inside the jet to that outside the jet. Black horizontal bands mark wavelength integration limits of 60 and 180 m and transparent boxes mark regions affected by spectral noise.

used as a proxy for the ratio of wave-wave to wave-mean flow interaction time scales (Polzin et al., in preparation, 2012). We find that Froude numbers are greatest, and thus wave-mean flow interactions most significant, in transects T2 and T3 where most the overprediction is found. However, it is difficult to ascertain the importance and effect of such wave-mean flow interactions. For example, the direction of energy transfer between the background flow and internal wavefield is dependent on the relative background current shear direction and phase velocity of the internal waves: we did not find a consistent signed background shear profile associated with regions of finescale overprediction. More detailed analysis is needed to ascertain the competing roles that wave-mean flow interactions may play to either accelerate or oppose the downscale energy cascade in the internal wavefield.

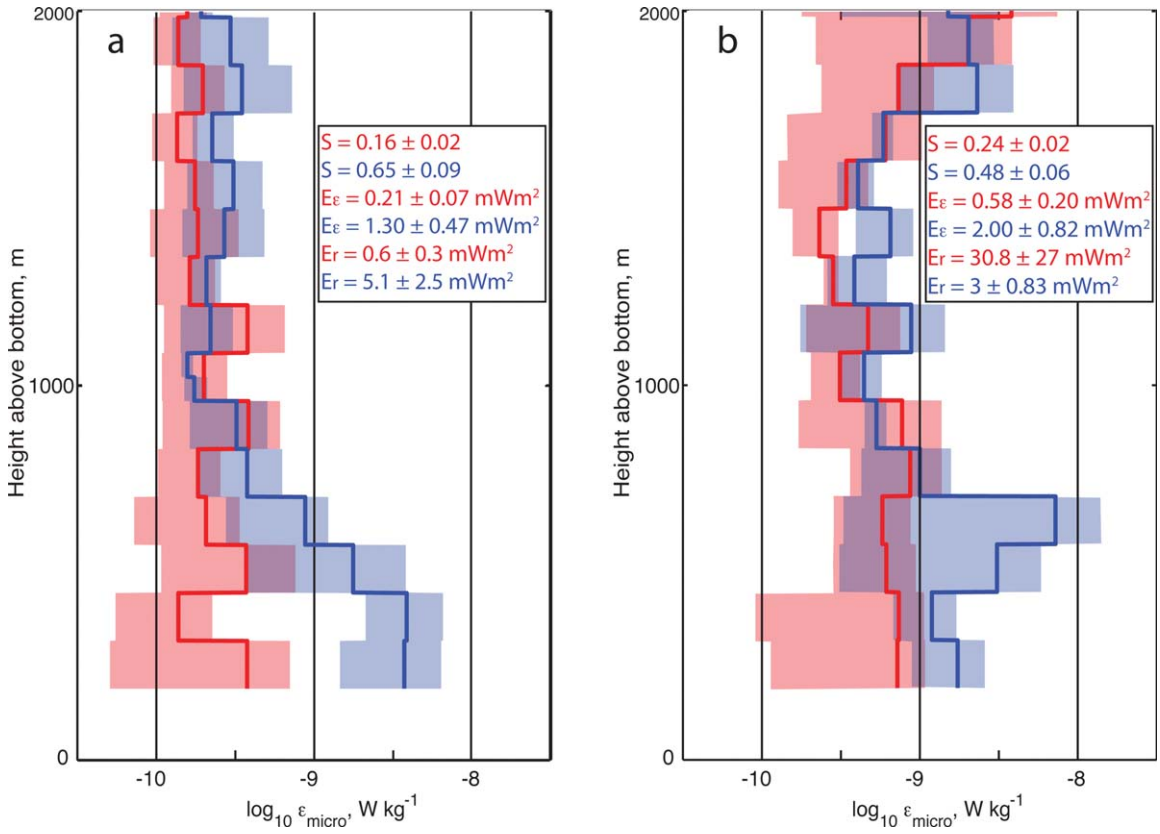

Figure 14. (a) Red = mean turbulent dissipations, computed from microstructure as a function of height above bottom for stations in transect T2 for which $S < 0.3$; blue = mean dissipation rates for stations in transect T2 within the inertial oscillation regime ($S > 0.3$). Shaded regions show 90% confidence limits computed from bootstrapping. Values show steepness, S, dissipated power in the bottom 1 km from microstructure, E_ϵ, and the predicted lee-wave energy flux, E_r, averaged over stations with $S < 0.3$ (red) and $S > 0.3$ (blue). The standard errors are also indicated. (b) As for Figure 14a, but for transect T4.

6. Conclusions

[39] In this study, we find evidence in support of our initial hypothesis that turbulent dissipation and diapycnal mixing in the ACC are both enhanced over rough bathymetry and sustained by the breaking of internal lee waves generated by ACC flow over topography. Turbulent dissipation rates are found to increase from $O\left(1 \times 10^{-10}\ \mathrm{W\ kg^{-1}}\right)$ in the southeast Pacific, to $O\left(1 \times 10^{-9}\ \mathrm{W\ kg^{-1}}\right)$ in the Scotia Sea. Regions of elevated dissipation generally coincide with both faster bottom current speeds and rougher small-scale topography, suggesting that the breaking of bottom-generated lee waves facilitates turbulent dissipation and mixing in the deep Southern Ocean. A detailed analysis of the properties of the internal wavefield provides further support for this hypothesis. We find that the spatial distribution of microstructure-deduced turbulent dissipation and mixing rates closely corresponds to the distribution of internal wave energy, and that elevated turbulent dissipation and mixing levels are associated with regions of relatively high-frequency and upward propagating internal waves. At the majority of measurement sites, turbulent dissipation rates are enhanced close to lee-wave generation sites, typically reaching $3 \times 10^{-9}\ \mathrm{W\ kg^{-1}}$ within 1 km of the seafloor. The occurrence of bottom-enhanced dissipation profiles has been related to the supercriticality of topography with respect to the lee-wave generation process, which is compatible with the occurrence of the inertial oscillation feedback mechanism proposed by *Nikurashin and Ferrari* [2010a].

[40] Application of nonlinear lee-wave radiation theory to our observations suggests that bottom-generated lee waves replenish the energy of the regional internal wavefield at rates of $O(0.1\text{–}1\ \mathrm{mW\ m^{-2}})$ in the southeast Pacific and $O(1\text{–}100\ \mathrm{mW\ m^{-2}})$ in the Scotia Sea. Although the spatial pattern of lee-wave radiation matches that of microstructure-derived turbulent energy dissipation in the deep ocean, only 10%–30% of the predicted lee-wave energy flux is observed to be dissipated within 1 km of the seabed. Thus, we find an order-of-magnitude discrepancy between the theoretical prediction of energy input by lee-wave generation to the region and the rate of turbulent dissipation. This discrepancy points to either a misrepresentation of the lee-wave generation process by the theory or to an alternative, nondissipative fate of the radiated energy. Some evidence in support of the latter scenario is provided by an observed enhancement of internal wave strain variance at vertical wavelengths $O(100\ \mathrm{m})$, which results in a systematic overprediction of turbulent dissipation rates by finescale parameterizations based on weakly nonlinear wave-wave interactions. This overprediction offers a

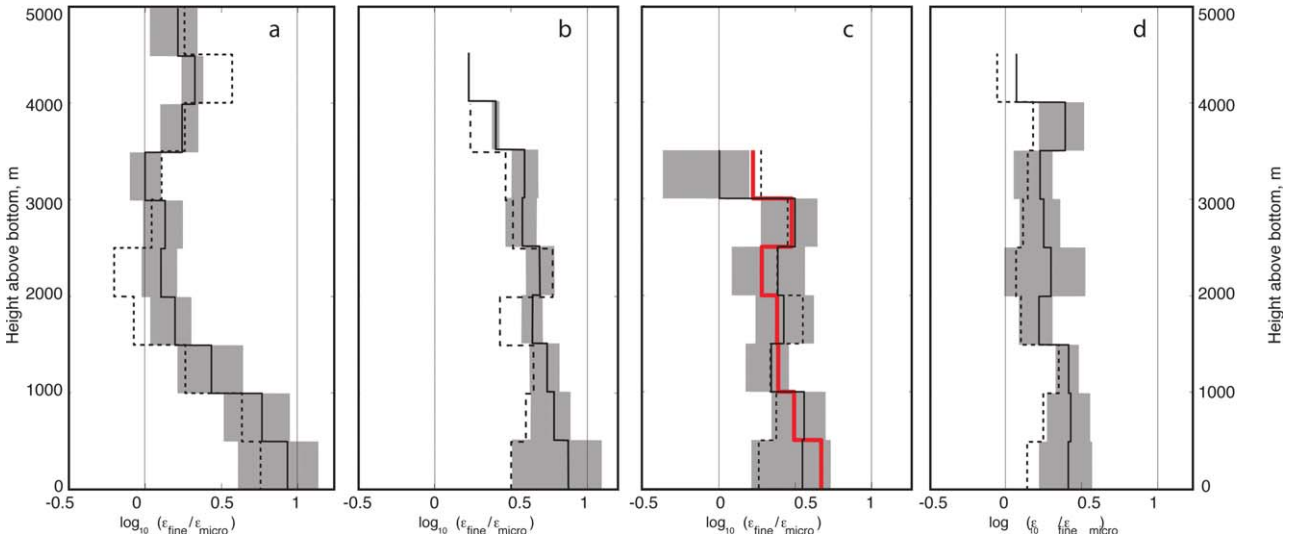

Figure 15. (a–d) Black solid lines = vertical profiles of transect-mean ϵ ratio as a function of height above bottom for transects T1, T2, T3, and T4, respectively. ϵ ratios are first computed as $\epsilon_{\text{fine}}/\overline{\epsilon_{\text{micro}}}$ where the overline represents mean microstructure dissipation over the same depth region used to compute strain and shear spectra. Subsequently, ratios are averaged into 500 m depth bins, and finally averaged across the transect. Shading represents 90% confidence interval calculated by bootstrapping. Dashed lines = results for 130–320 m shear and strain integration limits. Additional red line on Figure 15c = values computed from HRP2 measurements.

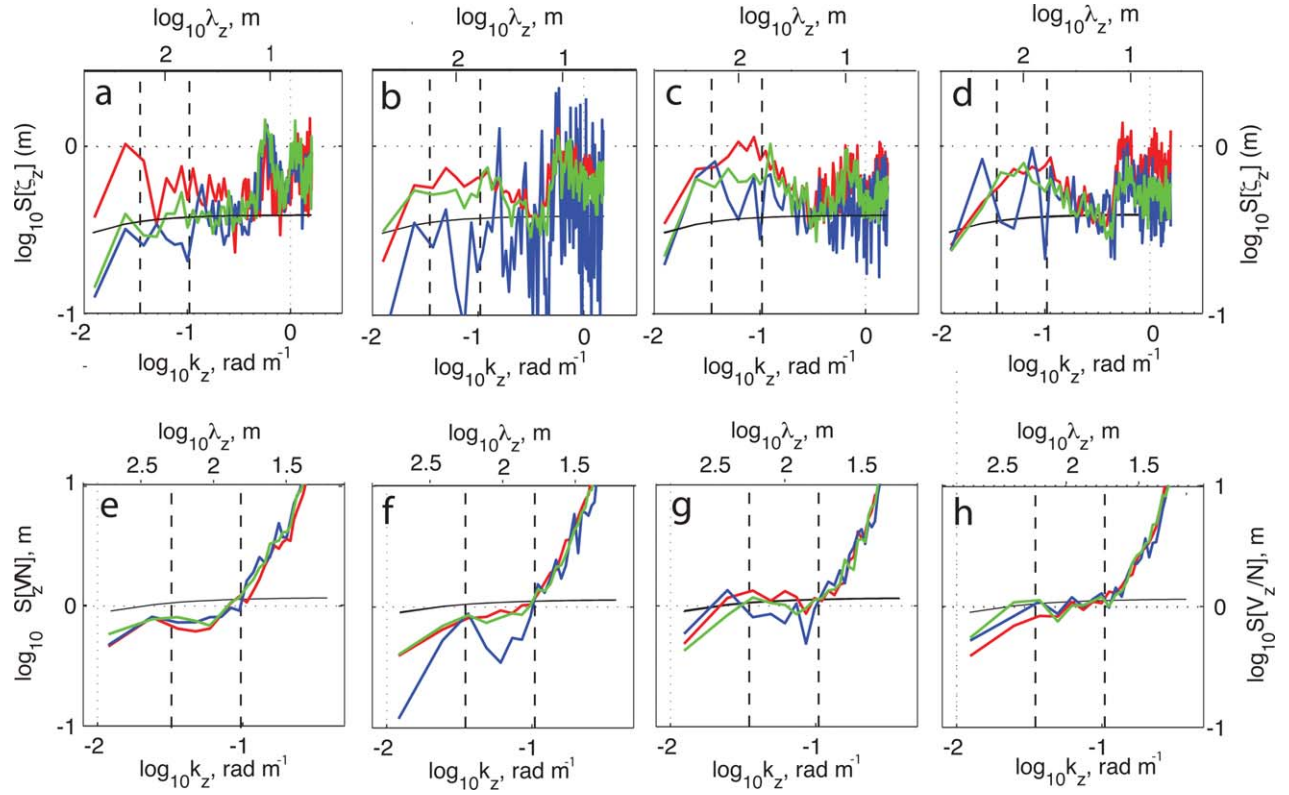

Figure 16. (a–d) Transect-mean strain spectra for transects T1–T4. Spectra are grouped according to finestructure over-prediction and normalized to GM height at a wavelength of 15 m to accentuate spectral shape. Blue: $\epsilon_{\text{fine}}/\overline{\epsilon_{\text{micro}}} < 1$; green: $1 <= \epsilon_{\text{fine}}/\overline{\epsilon_{\text{micro}}} < 3$; red: $\epsilon_{\text{fine}}/\overline{\epsilon_{\text{micro}}} >= 3$; black = GM spectral level; vertical dashed lines: vertical wavelength band (60–180 m) over which spectra are integrated for the calculation of ϵ ratios. (e–f) As for Figures 16a–16d but for corrected buoyancy normalized shear spectra for T1, T2, T3, and T4. Shear spectra are normalized to GM height at a wavelength of 60 m. Note that the transition to shear spectral noise occurs at lower wavenumbers in T1 than the other sections.

Table 1. Transect Mean Dissipation Rates $\left(\times 10^{-9}\ \mathrm{W\ kg^{-1}}\right)$ in the Bottom Kilometer for Microstructure and Finestructure-Deduced Values, Using Various Integration Limits for Shear and Strain Data

	T1	T2	T3	T4
$\epsilon_{\mathrm{micro}}$	0.26 ± 0.05	1.04 ± 0.23	2.34 ± 0.76	1.56 ± 0.54
ϵ_{fine} [a]	0.99 ± 0.17	1.71 ± 0.20	2.06 ± 0.34	2.55 ± 0.42
ϵ_{fine} [b]	1.00 ± 0.25	1.10 ± 0.14	1.70 ± 0.38	2.29 ± 0.39
ϵ_{fine} [c]	0.85 ± 0.17	1.24 ± 0.17	1.29 ± 0.22	1.81 ± 0.33
$\epsilon_{\mathrm{fine,HRP}}$ [d]			2.81 ± 0.75	

[a]The values are 60–180 m for both shear and strain.
[b]The values are 130–320 m for shear and strain.
[c]The values are 130–320 for shear and 30–150 m for strain [*Kunze et al*., 2006].
[d]The column labeled $\epsilon_{\mathrm{fine,HRP}}$ shows dissipation rates deduced from HRP2 velocities, using shear limits of $1/m_c$–180 m for shear and 60–180 m for strain. Errors represent the standard error in the mean. Note that finestructure values appear to underpredict microstructure-deduced dissipation estimates in transects T2 and T3, in contrast to results in Figure 4. This apparent inconsistency reflects the skewness of the abyssal microstructure data: the ratio of the transect mean ϵ values, as displayed in the table, tends to smear out any outliers present in the microstructure data. Estimates do not include values from the upper 100 m, and only include depths where both microstructure and finestructure were measured.

physical explanation for the comparatively large dissipation and mixing rates obtained previously by finestructure-based studies [e.g., *Naveira Garabato et al*., 2004]. We suggest that wave-mean flow interactions may play a role in the fate of the bottom-generated lee waves, though the extent to which this accounts for the discrepancy with the predictions of lee-wave radiation theory is unclear. The observed overprediction, found to be most pronounced in regions with high wave energy and near wave generation sites, may simply result from the invalidity of the assumption of weak nonlinearity, or from large-scale lee waves not having evolved fully to populate all wavelength scales.

[41] In summary, we conclude that the DIMES fine- and microstructure survey of a large sector of the ACC qualitatively endorses current views on the importance of bottom generated internal waves in determining the spatial distribution of small-scale turbulence and in their significant role in shaping the Southern Ocean circulation. The general alignment of our findings with those by *Waterman et al*. [2012] (Waterman et al., submitted manuscript, 2012) in a remote and distinct region of the ACC suggests that they are likely to be widely applicable across the Southern Ocean. In quantitative terms, however, our analysis poses some intriguing questions regarding the generation and evolution of the lee waves radiated as the ACC impinges on rough topography.

Table 2. As for Table 1, But Values Represent Mean Dissipation Rates at Depths Above 1 km From the Bottom[a]

	T1	T2	T3	T4
$\epsilon_{\mathrm{micro}}$	0.21 ± 0.01	0.29 ± 0.02	0.40 ± 0.06	0.92 ± 0.13
ϵ_{fine} [a]	0.49 ± 0.03	1.08 ± 0.05	0.80 ± 0.07	1.92 ± 0.24
ϵ_{fine} [b]	0.56 ± 0.07	0.89 ± 0.06	0.91 ± 0.13	1.77 ± 0.25
ϵ_{fine} [c]	0.55 ± 0.05	0.88 ± 0.06	0.90 ± 0.08	1.56 ± 0.19
$\epsilon_{\mathrm{fine,HRP}}$			0.96 ± 0.18	

[a]Estimates do not include values from the top upper 100 m.

Appendix A: Calculation of Internal Wavefield Parameters

A1. Spectral Integration Methods

[42] Finestructure-deduced turbulent dissipation rates, alongside internal wave energy, shear-to-strain variance ratios and the polarization ratios, require the integration of variance spectra (denoted by $S[x]$) over a specified wavenumber band. Following *Waterman et al*. [2012], we divide vertical CTD and LADCP vertical data profiles into 512 m, half-overlapping bins. As we are primarily interested in abyssal mixing, depth binning is started from the bottom of each cast. Data bins are detrended, tapered using a 10% $\sin^2$ window function with a correction for the loss of variance and Fourier transformed to produce power spectra. We choose to integrate both shear and strain spectra between 60 and 180 m. This wavelength bandwidth was chosen to minimize low wavenumber noise and high wavenumber dropoff in both shear and strain spectra (Figure 16). Using the same integration limits for both shear and strain ensures continuity between estimates and avoids errors associated with normalization to GM spectral levels. Tables 1 and 2 show the effect on transect-mean dissipation estimates of various integration bandwidths, which generally coincide within statistical uncertainties. Lower wavenumber ranges are likely affected by spectral dropoff. The robustness of inferred dissipation patterns on varying wavelength ranges is also reported by *Waterman et al*. [2012] and Waterman et al. (submitted manuscript, 2012).

[43] Integrated variance spectra, denoted by $S_i[x]$, are computed for four parameters.

[44] (i) Strain, ξ_z, is computed as the perturbation in the local stratification, such that $\xi_z = \frac{N^2 - N^2_{\mathrm{ref}}}{N^2_{\mathrm{ref}}}$, where N is the buoyancy frequency computed from CTD temperature, salinity, and density and N_{ref} is deduced using adiabatic leveling over a pressure range of 400 dbar [*Bray and Foffonoff*, 1981];

[45] (ii) Shear, V_z, is the depth gradient of horizontal current velocity, as measured by the LADCP. Zonal, u, and meridonal, v, velocity components are derived every 8 dbar, so are first linearly interpolated onto a regular depth grid of 8 m. Shear variance spectra, $S[V_z/N]$, and the counterclockwise, $S_{\mathrm{ccw}}[V_z/N]$, and clockwise components, $S_{\mathrm{cw}}[V_z/N]$, are subsequently computed using:

$$S[V_z/N] = S[u_z/N] + S[v_z/N],$$

$$S_{\mathrm{ccw}}[V_z/N] = \frac{(S[u_z/N] + S[v_z/N] + 2\mathrm{QS})}{2},$$

$$S_{\mathrm{cw}}[V_z/N] = \frac{(S[u_z/N] + S[v_z/N] - 2\mathrm{QS})}{2},$$

where the subscript, z, represents the depth gradient and QS is the quadrature spectrum [*Gonella*, 1972]. All shear-derived spectra were computed for both the LADCP upcast and downcast data, and then averaged. Shear spectra are normalized by the depth-mean stratification in the spectral

depth bin and corrected for loss of variance due to range averaging, depth binning, and instrument tilting as described for the velocity-inversion processing method in *Thurnherr* [2012]. We use a value of 8 dbar for the transmitted sound pulse length projected on the vertical, the receiver processing bin length, the interval of depth grid onto which single-ping piecewise-linear continuous profiles of vertical shear are binned and the preaveraging interval. For tilting corrections, a length scale, $d' = -1.2 + 0.0857 r_{\max} - 0.000136 r_{\max}^2$ is required. We use a range maxima, $r_{\max}$, of 90 m.

[46] (iii) LADCP horizontal velocity components, u and v.

[47] (iv) Height, $\mu = \frac{\gamma - \gamma_{\text{ref}}}{\gamma'_{\text{ref}}}$, where γ is neutral density, γ_{ref} is a smoothed background value, and γ'_{ref} its derivative with respect to depth. The value of γ is computed from CTD profile data using the Commonwealth Scientific and Industrial Research Organisation (CSIRO) neutral density code. γ_{ref} is calculated for each profile using a polynomial fit for overlapping segments of length 100 dB at the top of the profile, which is increased by 2 m every 8 m. This results in a smooth fit to the observed neutral density profile. Similarly, γ'_{ref} is estimated using a polynomial fit to γ'.

A2. Computing Internal Wave Parameters

[48] (1) **Turbulent dissipation,** ϵ_{fine}. The *Gregg* [2003] implementation of the finescale parameterizations is used to infer turbulent dissipation from finescale shear and strain variance:

$$\epsilon_{\text{fine}} = \epsilon_o \frac{N^2}{N_o^2} \frac{S_i[V_z/N]^2}{S_{i,\text{GM}}[V_z/N]^2} h(R_\omega) L(f, N), \text{ with}$$

$$h(R_\omega) = \frac{3(R_\omega + 1)}{2\sqrt{2} R_\omega \sqrt{R_\omega - 1}}, \text{ and}$$

$$L(f, N) = \frac{f \cosh^{-1}(N/f)}{f_{30} \cosh^{-1}(N_0/f_{30})},$$

where $\epsilon_o = 6.73 \times 10^{-10}$ m^2 s^{-3} and $N_o = 5.2 \times 10^{-3}$ rads^{-1} are the canonical GM dissipation rate and stratification, $S_{\text{GM}}[V_z/N]$ the GM 1976 shear spectrum and f_{30} the inertial frequency at 30° latitude [*Garrett and Munk*, 1976; *Gregg and Kunze*, 1991]. R_ω is the shear-to-strain variance ratio (see below).

[49] (2) **Internal wave energy,** E_{IW}. The total internal wave energy, E_{IW}, is computed as the sum of the horizontal kinetic energy, E_{KE}, and the potential energy, E_{PE}. E_{KE} and E_{PE} are deduced by integrating the kinetic and potential energy spectra, respectively, over vertical wavelengths in the range of 60–180 m. The kinetic energy is simply $E_{\text{KE}} = 1/2(S_i[u] + S_i[v])$. The potential energy is given by $E_{\text{PE}} = 1/2 N^2 S_i[\mu]$.

[50] (3) **Shear-to-strain variance ratio,** R_ω. The shear-to-strain variance ratio, $R_\omega = \frac{S_i[V_z/N]}{S_i[\xi_z]}$. Note, some values in Table 1 and 2 are computed using different integration limits for shear and strain spectra. In these cases, we compute R_ω by normalizing each spectra to the corresponding GM variance, such that $R_\omega = 3 \frac{S_i[\frac{V_z}{N}]/S_{i,\text{GM}}[\frac{V_z}{N}]}{S_i[\xi_z]/S_{i,\text{GM}}[\xi_z]}$.

[51] (4) **Polarization ratio,** R_{pol}. The polarization ratio, $R_{\text{pol}} = \frac{S_{i,\text{ccw}}[V_z/N]}{S_{i,\text{cw}}[V_z/N]}$

Appendix B: Calculation of Topographic Spectra

[52] Multibeam bathymetry data as shown in Figure 1b are used to compute topographic parameters used for theoretical lee-wave energy radiation calculations (section 4). The topography data, originally provided on a 0.002 degree grid, were despiked and all data shallower than 500 m removed. These processed data were next gridded into 2° latitude × 4° longitude boxes, which overlap by half their longitude and latitude. Box size was dictated by the requirement to be large enough for a sufficient number of topography tracks for spectral analysis, without compromising the homogeneity of the seabed roughness within a given box. An automated tracking algorithm was developed to identify and follow multibeam data tracks within each box, along eight directions (−63.4, −45.0, −26.6, 0, 26.6, 45.0, 63.4, and 90° from east). Tracks shorter than 33 data points were discarded and tracking was terminated if the step between data points was greater than 500 m. Tracks were interpolated using nearest neighbour interpolation onto regular intervals determined by the mean distance between data points along each track. Boxes with less than five tracks were discarded. Power spectral density estimates of bathymetric height were calculated using ensemble averaging with a 128 sample wide sin^2 normalized window which had no overlap, after first subtracting a linear fit. The variance of topographic height, H^2, was computed for each box by minimizing the averaged height spectra to that of the Goff and Jordan model spectrum, in log-log space. Finally, a second minimization was carried out on mean box spectra for each tracking direction, to determine the directionally dependent variables, k_o and μ, using the previously computed H for each box.

[53] **Acknowledgments.** The DIMES experiment is supported by the Natural Environment Research Council (NERC) of the U.K. and U.S. National Science Foundation. K.L.S. and J.A.B. are supported by NERC. We are grateful to A. Tate, who provided multibeam bathymetry data, M. Nikurashin, who assisted in lee-wave radiation analysis, and K. Polzin, who provided many helpful comments and advice. We also thank A. Bogdanoff, P. Courtois, K. Decoteau, X. Liang, and J.B. Sallée for their help in data collection and the valuable assistance and hard work of the crew and technicians on the *RRS James Cook*, the *RRS James Clark Ross*, and the *R/V Thomas G. Thompson*. Finally, we thank the manuscript reviewers for their helpful suggestions and comments.

References

Alford, M. H. (2003), Improved global maps and 54-year history of wind-work on ocean inertial motions, *Geophys. Res. Lett.*, *30*, doi:10.1029/2002GL016614.

Bell, T. H. (1975), Topographically generated internal waves in the open ocean, *J. Geophys. Res.*, *80*, 320–327.

Bray, N. A. and N. P. Fofonoff (1981), Available potential energy for MODE eddies, *J. Phys. Oceanogr.*, *11*, 30–46.

Garrett, C., and W. Munk (1976), Internal waves in the ocean, *Annu. Rev. Fluid Mech.*, *11*, 339–369.

Gill, A. E. (1982), Gravity waves in a rotating fluid, in *Atmosphere-Ocean Dynamics*, vol. *30*, pp. 247–315, Academic, London.

Gregg, M. C., and E. Kunze (1991), Shear and strain in Santa Monica Basin, *J. Geophys. Res.*, *96*, 16,709–16,719.

Gregg, M. C., T. B. Sanford, and D. P. Winkel (2003), Reduced mixing from the breaking of internal waves in equatorial waters, *Nature*, *422*, 513–515.

Goff, J. A., and T. H. Jordan (1988), Stochastic modeling of seafloor morphology: Inversion of sea beam data for second-order statistics, *J. Geophys. Res.*, *93*, 13,589–13,608.

Gonella, J. (1972), A rotary-component method for analysing meteorological and oceanographic vector time series, *Deep-Sea Res.*, *19*, 833–846.

Henyey, F. S., J. Wright, and S. M. Flatte (1986), Energy and action flow through the internal wave field: An eikonal approach, *J. Geophys. Res.*, *91*, 8487–8495.

Ledwell, J. R., L. St Laurent, J. B. Girton, and J. M. Toole (2011), Diapycnal mixing in the Antarctic Circumpolar Current, *J. Phys. Oceanogr.*, *41*, 241–246.

Kunze, E. (1985), Near-inertial wave propagation in geostrophic shear, *J. Phys. Oceanogr.*, *15*, 544–565.

Kunze, E., E. Firing, J. M. Hummon, T. K. Chereskin, and A. M. Thurnherr (2006), Global abyssal mixing inferred from lowered ADCP shear and CTD strain profiles, *J. Phys. Oceanogr.*, *36*, 1553–1576.

Lumpkin, R., and K. Speer (2007), Global ocean meridional overturning, *J. Phys. Oceanogr.*, *37*, 2550–2562.

Meredith, M. P., et al. (2011), Sustained monitoring of the Southern Ocean at Drake Passage: Past achievements and future priorities, *Rev. Geophys.*, *49*, RG4005, doi:10.1029/2010RG000348.

Munk, W., and C. Wunsch (1998), Abyssal recipes. II. Energetics of tidal and wind mixing, *Deep Sea Res.*, *45*, 1977–2010.

Naveira Garabato, A., K. Polzin, B. King, K. Heywood, and M. Visbeck (2004), Widespread intense turbulent mixing in the Southern Ocean, *Science*, *303*, 210–213.

Naveira Garabato, A., D. P. Stevens, A. J. Watson, and W. Roether (2007), Short-circuiting of the overturning circulation in the Antarctic Circumpolar Current Alberto, *Nature*, *447*, 194–197.

Naveira Garabato, A. C. (2009), RRS James Cook Cruise 29, 01 Nov–22 Dec 2008, SOFine cruise report: Southern Ocean finestructure, University of Southampton, UK, Natl. Oceanogr. Centre Southampton Cruise Rep. 35, 216 pp.

Naveira Garabato, A. C., A. P. Williams, and S. Bacon (2013), The three-dimensional overturning circulation of the Southern Ocean during the WOCE era, *Prog. Oceanogr.*, Submitted.

Nikurashin, M., and R. Ferrari (2010a), Radiation and dissipation of internal waves generated by geostrophic flows impinging on small-scale topography: Theory, *J. Phys. Oceanogr.*, *40*, 1055–1074.

Nikurashin, M., and R. Ferrari (2010b), Radiation and dissipation of internal waves generated by geostrophic motions impinging on small-scale topography: Application to the Southern Ocean, *J. Phys. Oceanogr.*, *40*, 2025–2042.

Nikurashin, M., and R. Ferrari (2011), Global energy conversion rate from geostrophic flows into internal lee waves in the deep ocean, *Geophys. Res. Lett.*, *38*, L08610, doi:10.1029/2011GL046576.

Oakey, N. S., (1982), Determination of the rate of dissipation of turbulent energy from simultaneous temperature and velocity shear microstructure measurements, *J. Phys. Oceanogr.*, *12*, 256–271.

Osborn, T. R. (1980), Estimates of the local rate of vertical diffusion from dissipation estimates, *J. Phys. Oceanogr.*, *10*, 83–89.

Orsi, A. H., T. Whitworth III, D. Worth, and W. D. Nowlin Jr. (1995), On the meridional extent and fronts of the Antarctic Circumpolar Current, *Deep-Sea. Res. I*, *42*, 641–673.

Polzin, K. L., and E. T. Montgomery (1996), Deep microstructure profiling with the High Resolution Profiler, paper presented at Microstructure Sensors Workshop, 23–25 Oct. 1996, Timberline Lodge, Mt. Hood, Oreg.

Polzin, K. L., J. M. Toole, and R. W. Schmitt (1995), Finescale parameterizations of turbulent dissipation, *J. Phys. Oceanogr.*, *25*, 306–328.

Roether, W., R. Schlitzer, A. Ptuzka, P. Beining, K. Bulsiewicz, G. Rohardt, and F. Delahoyde (1993), A chlorofluoromethane and hydrographic section across Drake Passage: Deep water ventilation and meridional property transport, *J. Geophys. Res.*, *98*, 14,423–14,345.

Sanford, T. B., J. H. Dunlap, J. A. Carlson, D. C. Webb, and J. B. Girton (2005), Autonomous velocity and density profiler: EM-APEX, in Proceedings of the IEE/OES Eighth Working Conference on Current Measurement Technology, University of Southampton, UK, IEEE. pp. 152–156.

Schmitt, R. W., J. M. Toole, R. L. Koehler, E. C. Mellinger, and K. W. Doherty (1988), The development of a fine- and microstructure profiler, *J. Atmos. Oceanic Technol.*, *5*(4), 484–500.

Scott, R., and Y. Xu (2009), An update on the wind power input to the surface geostrophic flow of the world ocean, *Deep-Sea Res. I*, *56*, 295–304.

Scott, R. B., J. A. Goff, A. C. Naveira Garabato, and A. J. G. Nurser (2011), Global rate and spectral characteristics of internal gravity wave generation by geostrophic flow over topography, *J. Geophys. Res.*, *116*, C09029, doi:10.1029/2011JC007005.

Sloyan, B. M. (2005), Spatial variability of mixing in the Southern Ocean, *Geophys. Res. Lett.*, *32*, L18603, doi:10.1029/2005GL023 568.

Smith, W. H. F., and D. T. Sandwell (1997), Global seafloor topography from satellite altimetry and ship depth soundings, *Science*, *277*, 1956–1962.

St. Laurent, L., A. C. Naveira Garabato, J. R. Ledwell, A. M. Thurnherr, J. M. Toole, and A. J. Watson (2012), Turbulence and diapycnal mixing in Drake Passage, *J. Phys. Oceangr.*, *42*, 2143–2152.

Thurnherr, A. M. (2012), The finescale response of lowered ADCP velocity measurements processed with different methods, *J. Phys. Oceanogr.*, *32*, 2882–2899.

Visbeck, M., (2002), Deep velocity profiling using lowered acoustic Doppler current profilers: Bottom track and inverse solutions, *J. Atmos. Oceanic Technol.*, *19*, 794–807.

Waterman, S., K. L. Polzin, and A. C. Naveira-Garabato (2012), Internal waves and turbulence in the Antarctic Circumpolar Current, *J. Phys. Oceanogr.*, *43*, 259–282.

Wu, L., Z. Jing, S. Riser, and M. Visbeck (2011), Seasonal and spatial variations of Southern Ocean diapycnal mixing from Argo profiling floats, *Nat. Geosci.*, *4*, 363–366.

Wunsch, C. (1998), The work done by the wind on the oceanic general circulation, *J. Phys. Oceanogr.*, *28*, 2331–2339.

Zika, J. D., B. M. Sloyan, and T. J. McDougall (2009), Diagnosing the Southern Ocean overturning from tracer fields, *J. Phys. Oceanogr.*, *39*, 2926–2940.